2015

Porosity Removal of CM247 Ni-base Superalloy using Thermal Heat Treatment without Applied Pressure

Chad Heinrich
University of Central Florida

POROSITY REMOVAL OF CM247 NI-BASE SUPERALLOY USING THERMAL HEAT TREATMENT WITHOUT APPLIED PRESSURE

by

CHAD HEINRICH
B.S. University of Central Florida, 2008

A thesis submitted in partial fulfillment of the requirements
for the degree of Master of Science
in the Department of Materials Science and Engineering
in the College of Engineering and Computer Science
at the University of Central Florida
Orlando, Florida

Fall Term
2015

Major Professor: Yongho Sohn

ABSTRACT

Blade and vane components made with Ni-base superalloys play a vital role in hot section of gas turbine engines. Removal of porosity in cast Ni-base superalloys is a critical process consideration since porosity from casting process can have deleterious effects on the performance and integrity of superalloy component. Still, the cost-efficient processing of Ni-base superalloys that are technologically acceptable, or superior, can contribute significantly to the life-cycle cost of gas turbine engines. The purpose of this thesis was to explore the possibility of eliminating the hot isostatic pressing cycle in a CM247 Ni-base superalloy processing. For cast CM247, conventional processing includes a hot isostatic pressing, which is primarily used to densify cast alloys by eliminating porosity. Two modified heat treatments without any applied pressure for CM247 were explored. Following these heat treatments, the porosity within each the sample was analyzed by electron microscopy. Results showed that HIP'ing removed 67.4% of the porosity from the as-cast CM247. The modified heat treatment examined in this study removed 97.9% of the porosity from the as-cast CM247. These experimental results were analyzed by considering the energetics of the HIP and modified heat treatments. Analysis demonstrated that most of the energy imparted on the casting for porosity removal can be due to temperature and not pressure, and justified how the modified heat treatments reduced porosity more effectively than the standard HIP cycle. Findings of this study can be immediately implemented for easier and more cost-effective processing of CM247 Ni-base superalloy.

This thesis is dedicated to my family; you inspire me daily. Thank you for your unbridled love.

ACKNOWLEDGEMENTS

I would like to express my genuine gratitude to my advisor, Dr. Sohn for giving me the opportunity to pursue this thesis. I would like to sincerely thank Le Zhou, Cynthia Klein, Dr. Raymond Snider and Dr. Allister James, Dr. Kevin Coffey and Dr. Helge Heinrich for making this thesis possible for me. I deeply appreciate the opportunities afforded to me by you all and will not forget them in my lifetime.

TABLE OF CONTENTS

LIST OF FIGURES

LIST OF TABLES

LIST OF ABBREVIATIONS/NOMENCLATURE

GB	Grain Boundary
γ	Gamma Phase
γ’	Gamma Prime Phase
HIP	Hot Isostatic Pressing
HT	Heat Treatment
SEM	Scanning Electron Microscope
SHT	Solution Heat Treatment
VIM	Vacuum Induction Melting

CHAPTER 1. INTRODUCTION

Gas turbines are becoming a greater part of the energy production market today. Nuclear power is an inexpensive and clean energy source but safety and long term environmental concerns have led to a declining use of this energy source. Renewables are gaining ground but are decades away from suppling most of the worlds electricity. Electricity production by burning coal releases significant amount of greenhouse gases and other pollutants. Coal is cheap but continues to be slowly phased out of the market due to environmental regulations. Natural gas resources are plentiful and operational emissions are relatively low making the gas turbine a viable option for large scale electricity production.

Ni-base superalloys play a vital role to the performance of gas turbines. Future electricity production should be cleaner and more cost advantageous compared to current electricity production. For the gas turbine, this requires higher firing temperatures for better performance and longer operating intervals for lower maintenance cost. These criteria could not be accomplished without Ni-base superalloys. This class of material has good corrosion resistance and high strength at elevated temperatures. Interestingly, flow stress, the stress where plastic deformation takes place, actually improves as exposure temperature increases, up to a certain point. For these reasons, all turbine rotating and stationary airfoils are made of Ni-base superalloys. Further, many combustor parts are made from Ni-base superalloys, and as performance requirements increase, more hardware will be made from Ni-base superalloys such as rotor discs and sealing parts.

The processing of Ni-base superalloys for turbine airfoil applications typically use the following process steps; Vacuum Induction Melting, Hot Isostatic Pressing, Solution Heat Treatment,

Aging Heat Treatments and if needed coating processes. The end result depends on the design of the material, material chemistry, and the parameters of each process step. Producing parts with desirable microstructural characteristics and without defects is the primary goal of Ni-base superalloy manufacturing. Internal defects, such as porosity, can cause parts to be scrapped if the defects are too numerous or located in undesirable locations within the casting. For this reason, the HIP process is applied to most Ni-base superalloy airfoil castings. HIP'ing is known to eliminate casting porosity and improve mechanical property scatter. HIP'ing simultaneously applies high temperature and high pressure to provide a driving force for pore closure. However, the HIP cycle adds a significant manufacturing cost and increases the hardware lead times. Also, improvements in the vacuum induction melting process have helped to ensure casting porosity is minimized during casting, before the HIP treatment. This thesis explores the hypothesis that the HIP cycle can be replaced with a cheaper modified heat treatment. Casting porosity was analyzed for samples processed using the current methods; as-cast, HIP and HIP + Solution heat treatment. Next, samples were exposed to six different modified heat treatments to determine the feasibility of replacing the HIP cycle with one of these modified heat treatments. After thermal processing, all the samples were polished viewed in a scanning electron microscope to search for microporosity in the microstructure. Next, the samples were etched using Glyceregia and viewed in the scanning electron microscope to study the gamma prime volume fraction and size. These are indicators of an alloy performance. The results were compared and contrasted and finally, recommendations were provided in the discussion section.

CHAPTER 2. LITERATURE REVIEW

2.1 Large Land Based Gas Turbine Engines

Large, industrial, land based gas turbine engines used for electricity production convert chemical energy into mechanical energy, which is then converted into electrical energy. Natural gas is becoming the fuel of choice due to its relatively low emissions and low price compared to fuel oil. Pending more stringent greenhouse gas emissions legislation, natural gas will gain a completive advantage over coal in the coming years.

Burning natural gas releases chemical energy, in the form of expanding hot gas, which is converted to work by the turbine section. The expanding hot gas imparts a force on the turbine blades which are attached to a rotor, causing the rotor to spin. The gas turbine rotor is bolted to an electrical generator which converts the mechanical energy from the gas turbine into electricity by electromagnetic induction. Following this process, the newest most efficient simple cycle power plants can obtain thermal efficiencies of more than 40% at a gross power output of more than 300 MW; enough electricity to power more than 330,000 American homes (EIA, 2015).

In a combined cycle power plant, thermal efficiency is improved by adding a heat recovery steam generator (HRSG) and a steam turbine to the cycle. The HRSG is a heat exchanger that captures waste heat from the gas turbine exhaust in order to create steam. The steam is then directed into a steam turbine which turns another electrical generator; thus, more electricity is produced in a combined cycle power plant for the same unit of fuel burned compared to a simple cycle power plant. Today, the most efficient combined cycle power plants can obtain thermal

efficiencies approaching 61% and a gross power output of more than 400 MW for 60 Hz application.

The cost of natural gas is by far the most expensive aspect of operating a gas turbine power plant. By improving power plant performance, owner operators pay less in fuel cost and/or generate more revenue which can increase profits and lower end user costs. A large part of the current power plant market demands more efficient, more powerful and more flexible combined cycle power plants; especially those customers in countries that do not have significant amounts of domestic natural gas resources like Korea, Japan or Europe.

The gas turbine industry continuously invests resources into research and development to improve gas turbine performance. It is expected that the next generation of large, land base gas turbines will achieve even greater performance as they become a bigger part of the world's electricity generators. High temperature materials, especially Ni-base superalloys, play a pivotal role in the economics of a gas turbine power plant. To show the connection between the need for high temperature materials and gas turbine performance, the following discussion will explore some of the thermodynamic parameters of a gas turbine power plant performance.

Gas turbine adiabatic thermal efficiency, according to the Brayton Cycle which describes a simple cycle gas turbine power plant, is dependent on the temperature ratio or the pressure ratio of the compressor as displayed in Equation (1) from (Quattrochi, 2006):

$$\eta_{th,Ideal} = 1 - \frac{1}{TR} = 1 - \frac{1}{PR^{\frac{\gamma-1}{\gamma}}} \quad (1)$$

where the compressor temperature ratio is given as $TR = \frac{T_{exit}}{T_{inlet}}$ and the compressor pressure ratio is given as $PR = \frac{P_{exit}}{P_{inlet}}$ and the specific heat ratio ($\frac{C_p}{C_v}$) is labeled as γ. This relationship is based

on the assumptions of equal pressure ratios between the compressor and turbine, constant air mass flow and fuel quality (constant $\frac{C_p}{C_v}$), and 100% operational efficiencies of all hardware. The ideal case in Figure 1 was plotted based on the relationship above. It can be seen that increasing the compressor temperature ratio or compressor pressure increases adiabatic thermal efficiency.

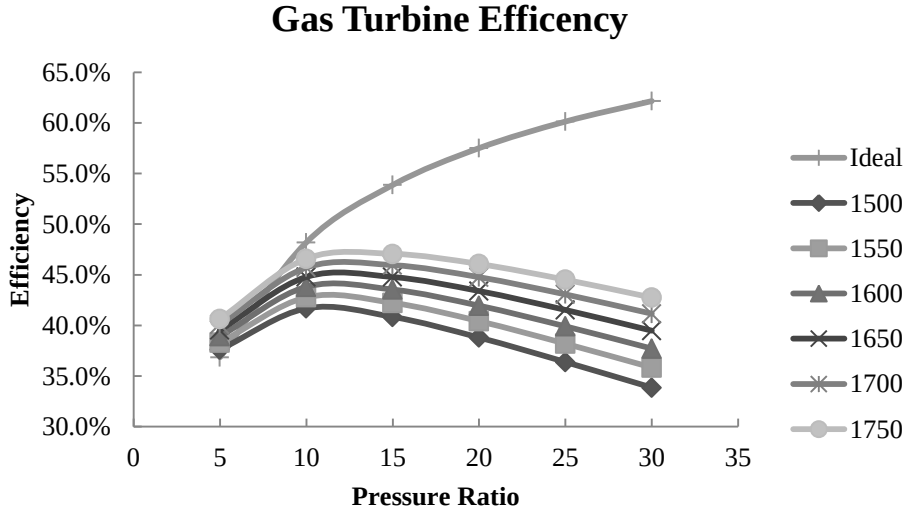

Figure 1: Gas Turbine efficiency for the ideal, adiabatic case and for η_t = 83% and η_c=77%. Each line represents a turbine inlet temperature of the value listed in the key

In reality, the individual component efficiencies are less than ideal ($\eta_t \neq \eta_c \neq 1$) which results in a deviation from the ideal case. The following equations help describe how component efficiencies can impact the overall gas turbine efficiency. The overall gas turbine efficiency is displayed in Equation (2):

$$\eta_{th} = \frac{Work_{turbine} - Work_{compressor}}{Heat_{in}} \tag{2}$$

The turbine section work is displayed in Equation (3):

$$Work_{turbine} = \eta_t \dot{m}_t R T_3 \frac{\gamma - 1}{\gamma} (1 - r_t^{\frac{-\gamma+1}{\gamma}}) \tag{3}$$

where η_t is turbine efficiency, $\dot{m}_t$ is mass flow through the turbine, R is c_p-c_v, T_3 is the turbine inlet temperature, $\boldsymbol{\gamma}$ is c_p/c_v and r_t is the turbine pressure ratio. Next, Equation (4) represents the compressor section work:

$$Work_{compressor} = \frac{1}{\eta_c}\dot{m}_c R T_1 \frac{\gamma}{\gamma - 1}(r_t^{\frac{\gamma-1}{\gamma}} - 1) \tag{4}$$

where η_c is compressor efficiency, $\dot{m}_c$ is mass flow through the compressor, T_1 is the compressor inlet temperature and r_c is the compressor pressure ratio. Next, the heat added by the combustor section can be described by Equation (5):

$$Heat_{in} = \dot{m}_h R T_2 \frac{\gamma}{\gamma - 1}(\frac{T_3}{T_2} - 1) \tag{5}$$

where $\dot{m}_h$ is mass flow through the combustor and T_2 is the combustor inlet temperature. By plugging Equations (3), (4) and (5) back into Equation (2), assuming all mass flows and pressure ratios are equal and that $\boldsymbol{\gamma}$ = 1.4 (for atmospheric air) for all calculations, gas turbine efficiency can be estimated as shown in Figure 1.

Figure 1 displays the general trend that actual gas turbine efficiency increases and then decreases as the pressure ratio is increased for a given firing temperature. This is because as the pressure ratio increases, the cooling air usages increases, to maintain metal temperatures, which decreases gas turbine performance. Also, as Mach numbers increase with increasing mass flow, to achieve increased pressure ratios, tip losses are more significant and negatively impact gas turbine performance.

It is important to note that increasing turbine inlet temperature will always result in better gas turbine efficiency for a given pressure ratio. This is a key point for superalloy development. Gas turbine designers desire to increase the turbine inlet temperature to improve gas turbine

performance; thus, they need materials that perform at high temperatures and in harsh environments. Superalloys, especially Ni-base superalloys, are perfectly suited for this type of application.

2.2 Superalloys

Superalloys are a class of materials prescribed to operate in high temperature, often at greater than 0.7 T_m, high stress, often greater than 250 MPa, and corrosive environments for long periods of time. They are widely used in aero and land based gas turbines because they are uniquely equipped to operate in these conditions. Simply put, modern gas turbine engines would not exist without superalloys.

Superalloys are grouped into three categories: iron (Fe) based, cobalt (Co) based or nickel (Ni) based, meaning the major solvent element is either Fe, Co or Ni, respectively. Superalloy development has been closely related to the development gas turbine engines because superalloys have excellent high temperature performance and corrosion resistance. As the demand for more powerful and fuel efficient gas turbines increases, so does the research into ways to improve superalloy performance to match these requirements. This symbiosis began with the advent of the jet engine in the 1930s and continues to this day.

Nickel based superalloys are the most widely used superalloy compared to Fe or Co based. These alloys are often exposed to gas path temperatures in excess of 1500 ºC, which is above the melting temperature of nickel at 1455 ºC. Therefore, components are often reliant on thermal barrier coatings and sophisticated cooling schemes to maintain acceptable base-metal

temperatures. For industrial gas turbine hardware, which requires long service lives more than absolute performance, base metal temperatures are usually closer to 1000 ºC.

Nickel base superalloys are widely used because of their high temperature performance and oxidation resistance as observed in Figure 2.

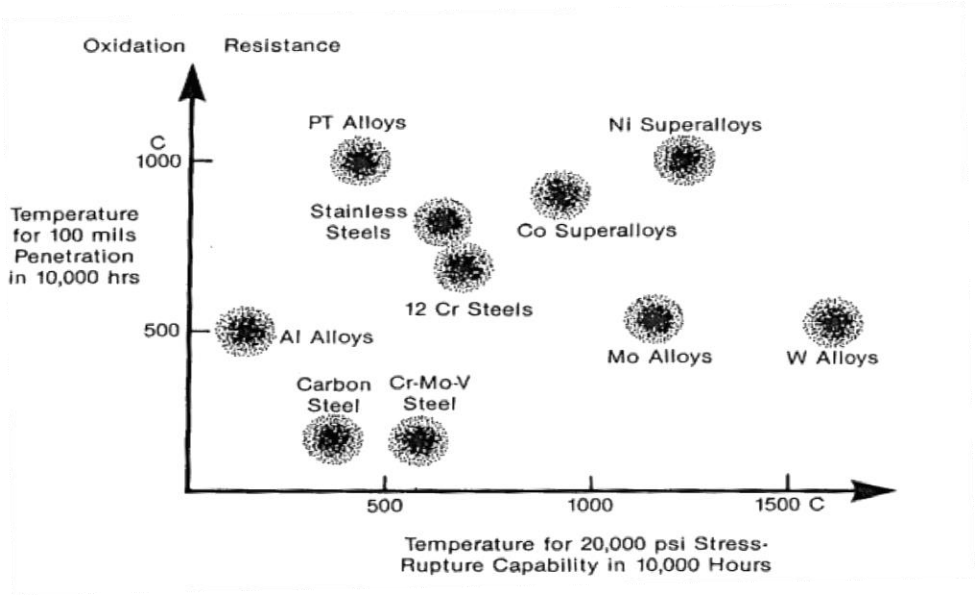

Figure 2: Oxidation resistance vs. high temperature capabilities for various classes of materials (Sims, Stoloff, & Hagel, 1987)

Nickel base superalloys achieve their characteristics for a combination of reasons. Ni has a face centered cubic (FCC) structure up to its melting temperature. FCC structures are closed packed, giving the highest packing efficiency possible, 0.74. A high packing efficiency results in higher coordination number and more slip systems, which means FCC materials have good ductility. Arguably the most significant difference between Ni-base superalloys and Co or Fe based superalloys is the ability for Ni-base superalloys to readily form the gamma prime phase (γ'), Ni_3 (Al, Ti, Nb, Ta). Researchers identified the benefits of this precipitate phase and began focusing on improving the high temperature capabilities of Ni-base superalloys by managing the

properties of the gamma prime phase. Along with superior alloy performance, Ni tends to be cheaper than Co which gives Ni an advantage during alloy research, design and ultimately selection.

2.2.1 Microstructure & Strengthening

Ni-base superalloy microstructures are primarily made up of a gamma (γ) matrix phase with a high volume fraction of the precipitating gamma prime phase (γ'). The γ phase is primarily Ni along with lesser amounts of Al. The gamma phase has a disordered FCC structure shown in the left image of Figure 3. Any of the Ni or Al atoms can be located anywhere in the FCC lattice; there are no preferential sites or long range order.

The γ' phase takes the form of a primitive cubic $L1_2$ structure with Al atoms at the cube corners and Ni atoms at the face center locations as seen in the right image of Figure 3. Because of the preferred site occupancy of Al and Ni (preferred bonding), this phase has long range order and is, therefore said to be an ordered phase. The γ' phase is the primary Ni-base superalloy strengthener by precipitation hardening. Typical forms of the γ' phase include Ni_3Al or Ni_3Ti (Reed, 2006).

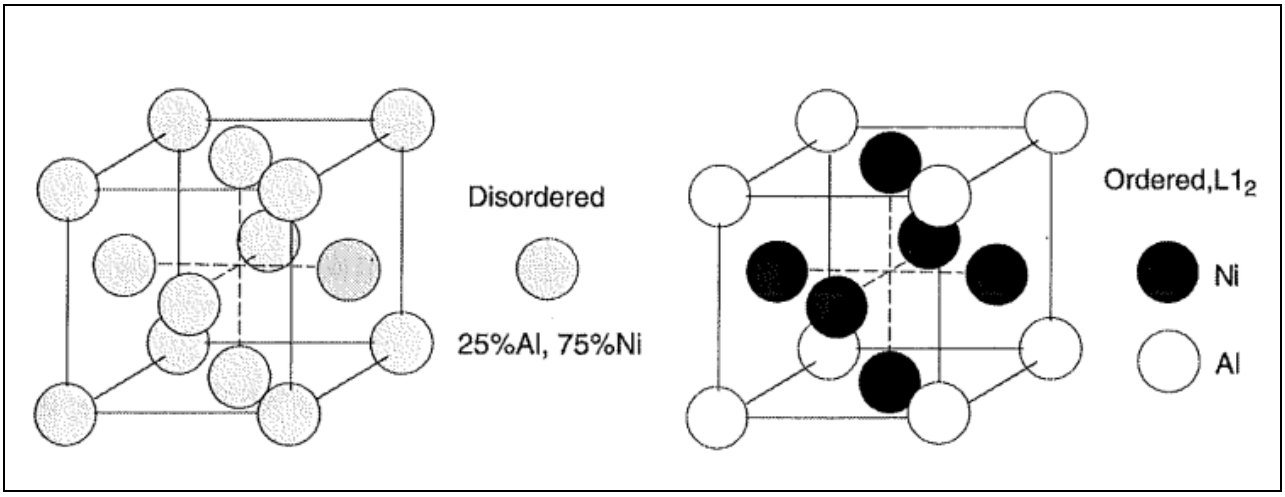

Figure 3: Disordered (left) vs. ordered (right) FCC gamma prime matrix (Reed, 2006)

Ni-base superalloys are primarily strengthened by three mechanisms: solid solution strengthening, precipitation hardening and grain boundary strengthening.

2.2.1.1 Solid Solution Strengthening

Solid solution strengthening can occur when, following the Hume-Rothery rules, the atomic size difference of the solvent and solute atoms are <15%, the solvent and solute has the same crystal structure, similar valences and similar electro-negativities. For Ni-base superalloys, solid solution strengthening occurs when solvent atoms (Ni) are replaced by solute atoms (ex. Co, Cr, Mo, W) in the FCC lattice. This is known as substitutional solid solution.

High temperature strength, gained from solid solution strengthening, is caused by impeding dislocation movement through the lattice. This occurs primarily due to size and modulus effects from the solute atoms. Depending on the size of the solute atom compared to solvent atom, a compressive or tensile stress field is created due to the lattice distortion and this stress field obstructs dislocation movement. The modulus effect is due different atoms having different

moduli. If the local modulus, or hardness, of the matrix changes, then local stress fields are created. These local stress fields impede dislocation movement in the lattice (Weaver, 2011).

2.2.1.2 Precipitation Hardening

Precipitation strengthening is the major strengthener in Ni-base superalloys. The intermetallic γ' phase precipitates in the γ matrix at relatively high temperatures. Ni-base superalloy go through solution and aging heat treatments to precipitate the γ' phase and to achieve the desired volume fraction and morphology of the γ' phase which are important for material performance. Figure 4 shows the strong relationship between the γ' phase volume fraction and superalloy material rupture life, as a function of temperature.

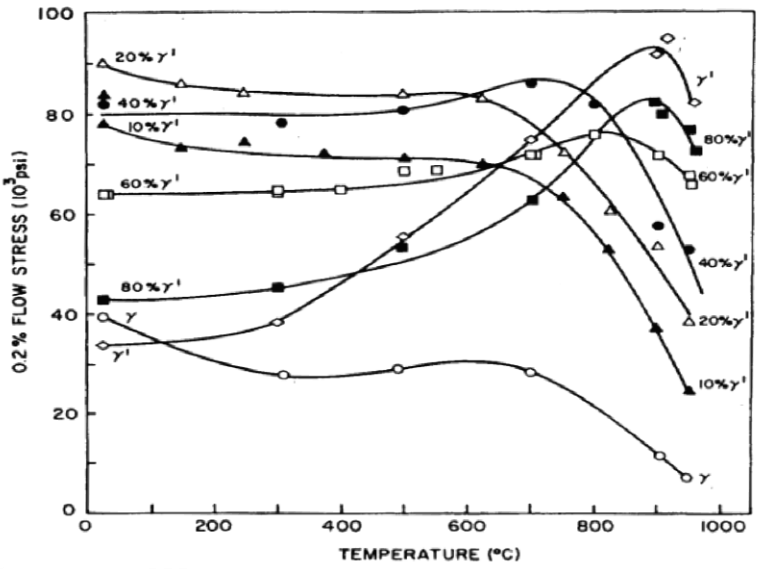

Figure 4: Effect of gamma prime volume fraction on rupture life of some Ni-Cr-Al alloys (Sims, Stoloff, & Hagel, 1987)

A Ni-base superalloy can contain more than ten individual elements. At high temperatures, some of these elements form intermetallic compounds such as Ni_3Al or Ni_3Ti known as the gamma

prime (γ') phase. These particles have a closely matching lattice parameter with the parent γ phase which results high coherency between the two phases. This means that the number of atomic bonds are maintained even when the precipitate size is different than the parent matrix which leads to lattice strain between the γ and γ' phases. This lattice strain, shown in Figure 5, hinders dislocation movement.

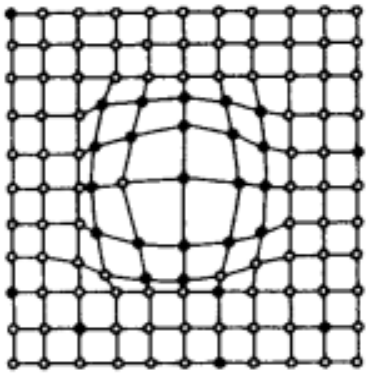

Figure 5: Lattice strain created by a coherent precipitate particle (Sims, Stoloff, & Hagel, 1987)

Figure 6 shows that the creep rupture life increases with decreasing lattice mismatch due to increased coherency. This is because the coherent γ' phase is ordered and remains stable at elevated temperatures.

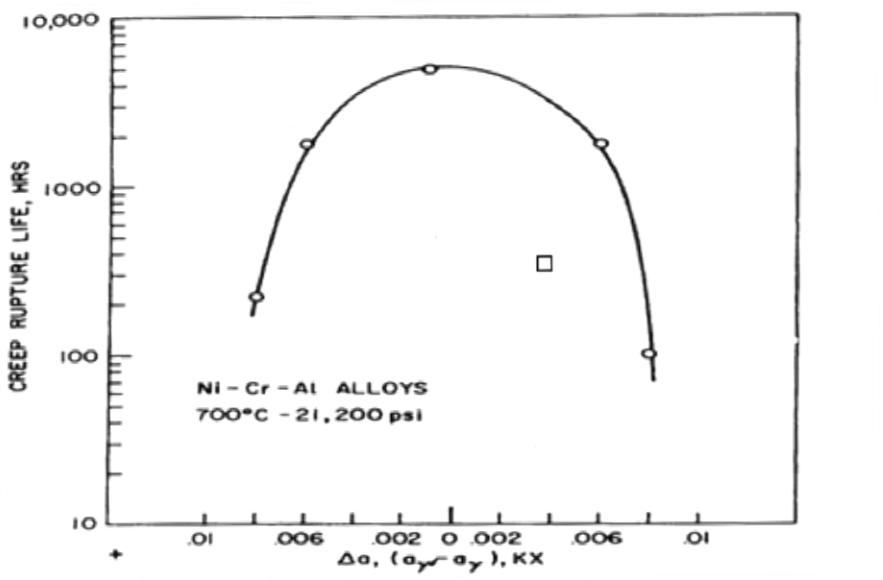

Figure 6: Effect of coherency on creep rupture life (Sims, Stoloff, & Hagel, 1987)

As mentioned previously, the γ' phase displays long rang order almost up to its melting temperature (Reed, 2006). Ordered structures have stacking fault defects, such as anti-phase boundaries (APB), which can impede dislocation movement. Anti-phase boundaries are formed by dislocation cutting and result in Ni-Ni or Al-Al bonds rather than the preferred, lower energy Ni-Al bonds. Therefore, to return the system to the lowest energy, another dislocation must follow the first dislocation so the Ni-Al bonds will form again. These dislocation pairs are called super dislocations as seen in Figure 7. High energy is required for them to move through the γ' lattice.

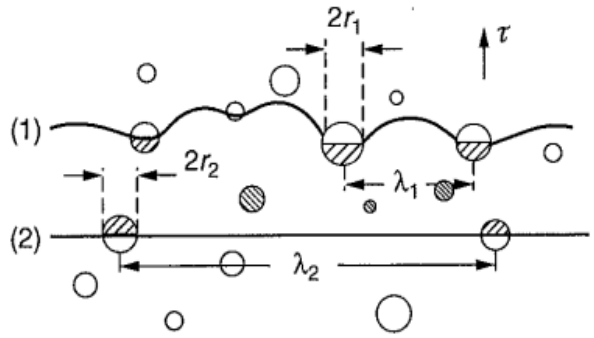

Figure 7: Super dislocation shearing particles of gamma prime (Reed, 2006)

At high temperatures, the γ' phase begins to coarsen and loose coherency with the γ phase. As the γ' particles increase in size the dislocations tend to bow around them instead of cutting through them. This helps to explain why the γ' phase flow stress increases with temperature up to about 700ºC as seen in Figure 4. This plot also shows that increasing the γ' volume fraction results in greater strength.

2.2.2 Processing of Superalloys

2.2.2.1 Vacuum Induction Melting (VIM)

Superalloy ingots are commonly produced by Vacuum Induction Melting (VIM); whereby, elements are heated, by induction, in a crucible under a vacuum. The vacuum ensures oxygen, hydrogen and other undesirable gases are removed from the molten metal. The molten metal is then poured into ingots under an inert atmosphere in preparation for investment casing. Figure 8 shows an example of a VIM furnace.

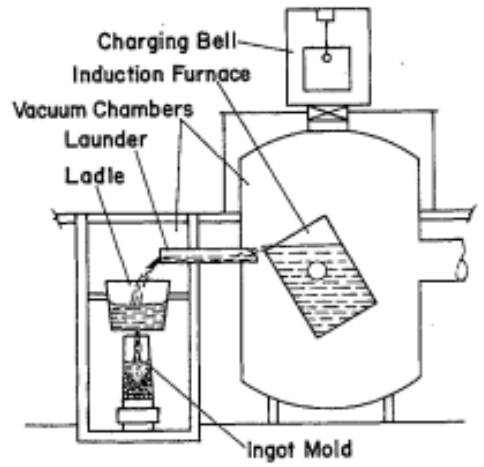

Figure 8: Example of vacuum induction melting (Sims, Stoloff, & Hagel, 1987)

Molten metal will absorb gas within the furnace during melting. The solubility of gas in metals can be calculated using Sievert's relation shown in Equation (6) (Smallman & Ngan, 2007):

$$\text{Gas Concentration} = K \cdot (p(\text{gas}))^{1/2} \quad (6)$$

Where K is a temperature dependent variable and p(gas) is the partial pressure of the gas within the furnace atmosphere. This relation shows the gas concentration within a melt decreases during cooling because pressure decreases with temperature. At some point during cooling, the gas will no longer be soluble in the liquid metal. When this happens, gas bubbles can form leading to internal porosity. One way to mitigate this effect is to remove the highly reactive gas molecules from the furnace during processing. This is accomplished by purging the furnace with an inert gas and pulling a vacuum on the furnace; hence the name, vacuum induction furnace. Most commercial superalloys today are melted and cast using the vacuum induction melting technique for this reason.

2.2.2.2 Investment Casting

Gas turbine airfoils are typically cast using the near net shape process of investment casting. Investment casting is expensive and involves multiple steps to complete as seen in Figure 9.

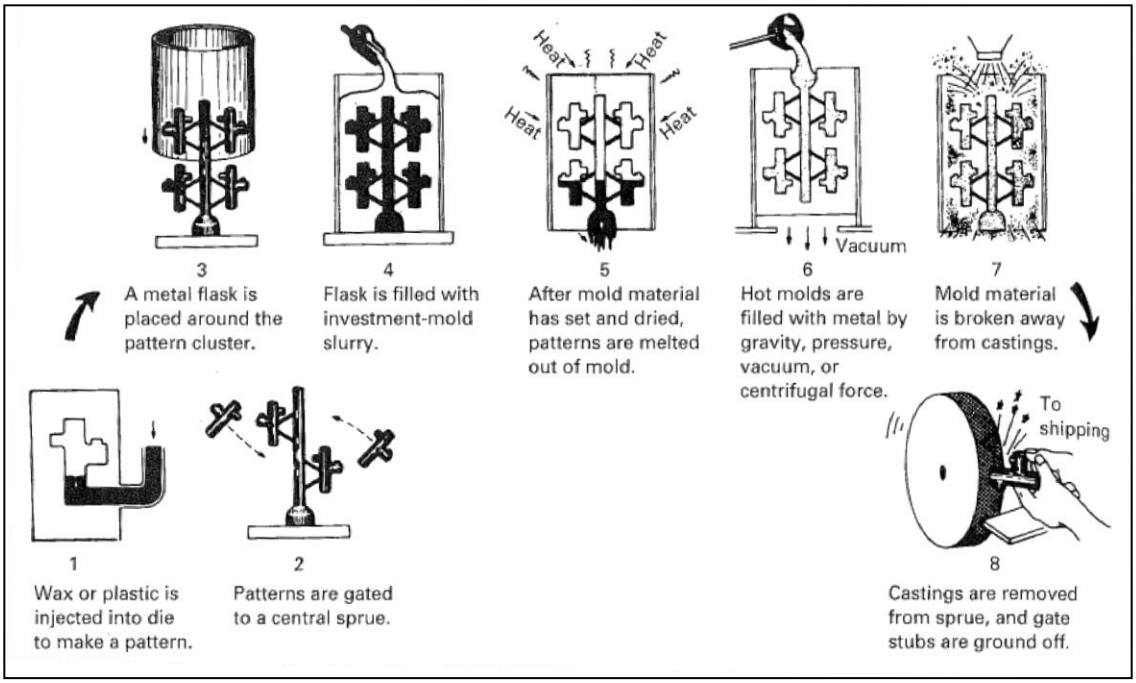

Figure 9: Schematic of the investment casting process (Black & Kohser, 2008)

First, a die is created which is the negative shape of the desired blade or vane. A grain selector will be incorporated into the die if columnar or single crystal airfoils are being manufactured. Next, plastic is injected into the die around a ceramic core which is used to create a pattern of the internal cooling passages. Multiple patterns are combined or gated together and coated with ceramic slurry and refractory elements. This process is repeated multiple times until the desired shell thickness is achieved. The plastic is then removed from the molds using acid. Finally, molten metal is poured into the heated molds under a vacuum. If the parts will be directionally solidified, the solidification rate will be precisely controlled to ensure the solidified grains are

oriented in the <001> direction. Once the metal is cool enough, the mold shells are removed, the molds are separated and any excess metallic material, namely the gating, is removed. Although expensive, the investment casting process is used because very intricate airfoil geometry and cooling passages can be produced. Also, machining superalloys is difficult due to their high strength. Reducing the amount of machining and waste by casting the blades and vanes to near net shape is advantageous.

2.2.3 Processing Hot Isostatic Pressing (HIP)

Hot isostatic pressing is an expensive process that is performed in an explosion proof pressure vessel due to the high pressures used. The HIP process occurs post casting and is usually combined with the solution heat treatment for economic reasons. During the HIP cycle, production parts are heated in an inert environment to high temperatures, avoiding incipient melting, under high pressure, often >100 MPa (Sims, Stoloff, & Hagel, 1987). The high pressure gas reacts on the surface of the material pressing it in all directions which causes a volume reduction thus, densification. The main benefit of the HIP processing of superalloy cast parts is to close internal microporosity remnant from the investment casing process. By removing internal porosity, creep life (Figure 10) and fatigue life (Figure 11) are improved. Additionally, these figures also show that HIP'ing also tends to reduce the scatter of mechanical properties between specimens.

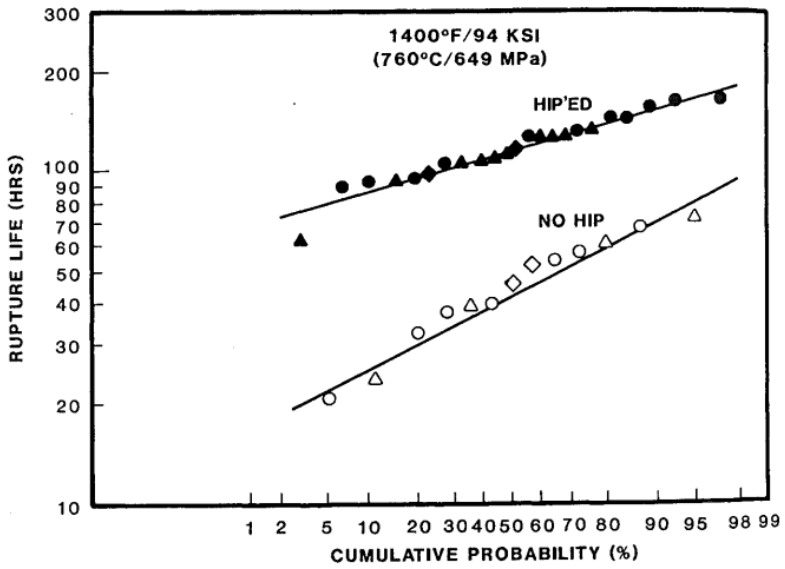

Figure 10: Improved creep life due to reduced internal porosity (Sims, Stoloff, & Hagel, 1987)

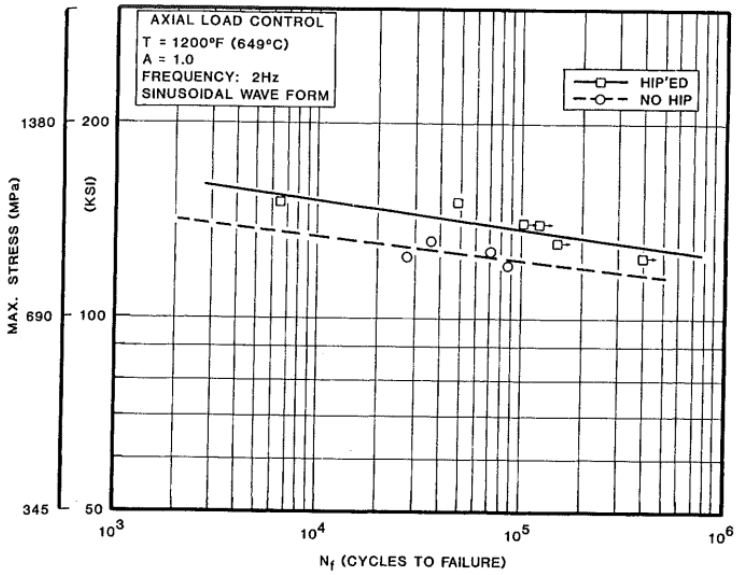

Figure 11: Showing fatigue life improvement due to HIP (Sims, Stoloff, & Hagel, 1987)

HIP processing effectively removes porosity within a casting by a combination of deformation, creep and diffusion processes. Depending on the HIP'ing parameters, these processes can

individually dominate the densification rate. Figure 12 shows this relationship with respect to the applied HIP pressure at a constant temperature.

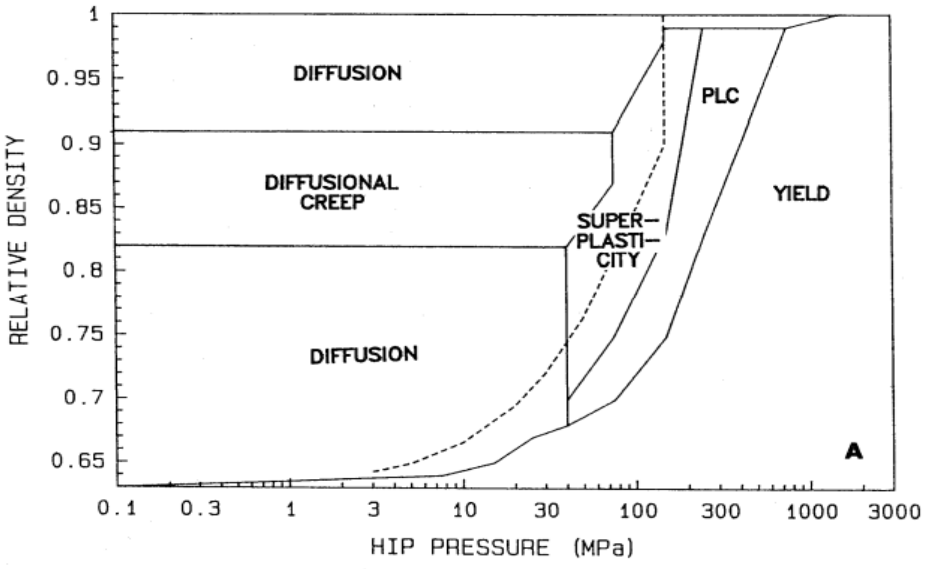

Figure 12: HIP map created for Rene 95 at 1121°C (Borofka, R.D., & Tien, 1988)

2.2.4 Porosity

Internal porosity typically forms in the interdendritic region of the microstructure during solidification. Porosity mainly forms either due to entrapped gas bubbles or due to shrinkage (Whitesell III, 2002). Gas bubbles form when gas reaches a solubility limit and nucleate. Depending on the local pressure of the melt and partial pressure of the gas, the bubble will either diffuse back into the liquid metal if the partial pressure is equal or less than the melt pressure or will remain to form porosity if the partial pressure of the gas is higher than the melt pressure. Shrinkage occurs during solidification when regions of the microstructure are cut off from the liquid metal by secondary or tertiary dendritic arms. Shrinkage can be controlled with solidification rates which controls the dendritic structure or by proper gating to ensure enough

liquid metal is supplied to all areas of the casting. Figure 13 shows the relationship between solidification rate and porosity formation.

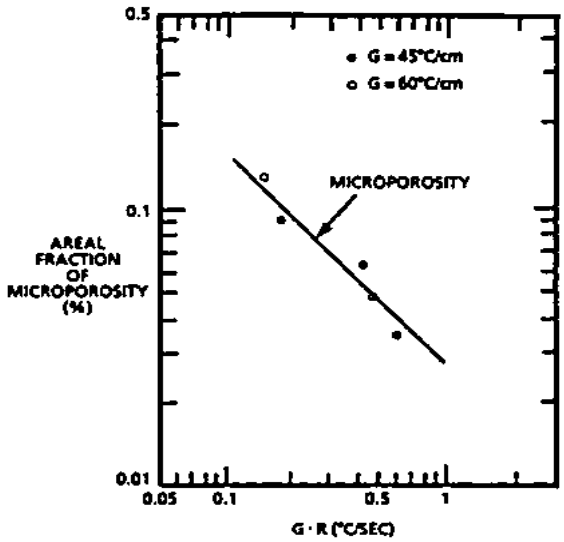

Figure 13: Microporosity vs. cooling rate (Tien & Caulfield, 2015)

Microporosity has a detrimental effect on mechanical properties. Pores act as stress risers which cracks tend to nucleate from during loading. Figure 14 shows how the creep life of a superalloy is negatively affected by porosity.

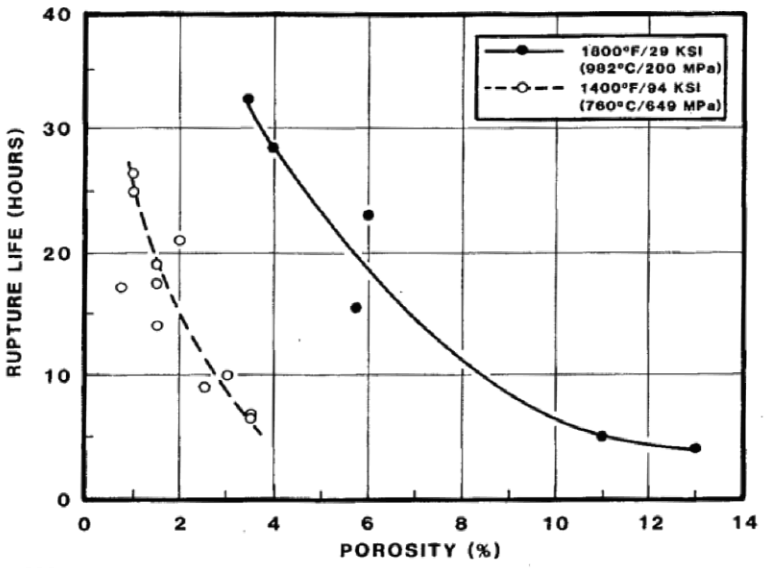

Figure 14: Porosity vs creep life (Sims, Stoloff, & Hagel, 1987)

Porosity is reduced by controlling the amount of gaseous elements available to form porosity. For example, low vapor pressure gases are removed during VIM. Also, HIP'ing can be employed to fully remove and densify castings. The high temperature employed during HIP'ing tends to dissolve gaseous elements in the metal while the high pressure helps to collapse any porosity that does form with the hopes that the gaseous elements will migrate to the outer surfaces of the casting and into the surrounding atmosphere. Porosity can also be controlled with the alloying elements used to make the alloy. It has been observed that Al, Ti and Co facilitated more porosity compared to Cr which has been reported to minimize porosity formation (Lecomte-Beckers, 1988).

CHAPTER 3. THERMODYNAMIC ANALYSIS OF PORE CLOSURE

The following sections discuss the energy required to reduce internal porosity. Internal porosity has deleterious effects on the mechanical properties of a Ni-base superalloy as described in section 2.2.4. The following sections first presents calculations used to determine the minimum amount of energy required to remove porosity in cast CM247. Then, estimations of the actual energy input into the castings are made using HIP'ing parameters for CM247 in the calculations. The calculations made in sections 3.1 and 3.2 provide an estimate of the amount of energy required to reduce porosity by using two different analytical approaches. The first approach, in section 3.1, uses a relationship between material yield stress and hardness. The second approach, in section 3.2, calculates the total energy required to reduce the surface area of a single pore. The two approaches are used to compare and contrast the validity of each method to each other and to the energy input by the HIP process in section 3.3.

3.1 Energy Required for Pore Closure - Yielding

The force required to cause yielding of one pore in the sample was estimated using the relationship between material hardness (H) and yield strength (σ_y) in Equation (7) from (Meyers & Chawla, 2009):

$$\frac{F}{A} = H = 3\sigma_y \tag{7}$$

This equation was derived to relate the downward force, F, imparted by a hardness measurement indenter and the cross sectional area, A, of the indenter. This provides a relationship where only

the force is unknown in this calculation. Experiments by (Zhang, Li, & Zhang, 2011) confirm the relationship in Equation (7) is a good approximation.

From optical microscopy, the observed average porosity diameter from the "as-cast" samples was approximately 15 μm as seen in Figure 15.

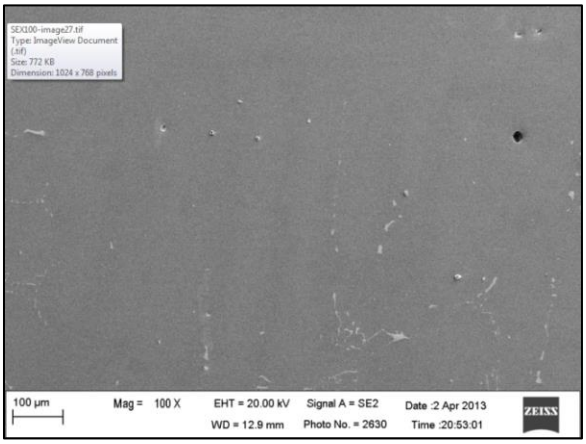

Figure 15: Porosity size example

The yield strength of CM247 at 760^{o}C is 960MPa (Huang & Koo, 2004). Assuming the force acts on a spherical pore cross sectional area and solving Equation (7) for F, the force required to close a single 15μm pore is calculated to be 0.509N. Assume that complete closure of the pore results in the material traveling one radius length of the pore. If this is done, then the work required to close a single pore can be estimated by Equation (8) below.

$$Work = Force \cdot distance \tag{8}$$

Plugging in a force of 0.509N and radius of 7.5μm, the amount of work energy required to close a single spherical pore is calculated to be.

$$Work = F \cdot r = 0.509N \cdot 7.5\mu m = 3.82\ x\ 10^{-9} KJ$$

Next, the total work required to close all the pores in the sample was estimated. To estimate this, the following assumptions are required:

- The as-cast average porosity percent was measured to be 0.304% in the as cast sample
- The as-cast average porosity percent was measured to be 0.099% in the HIP sample
- The average diameter of all the porosity measured in the as cast samples was 15 μm. Therefore, in the calculations, all pores are assumed to have a 15 μm diameter.
- The sample dimensions were = 0.013 m x 0.025 m x 0.006 m which results in a volume of 2.048 x 10^{-6}

The volume of a pore can be calculated using Equation (9) below.

$$V_{pore} = \frac{4}{3}\pi r^3 = 1.8 \cdot 10^{-15} m^3 \quad (9)$$

The as-cast sample volume was reduced by the difference between the as-cast and post HIP average porosity percent. Therefore, the post HIP sample volume is calculated using Equation (10).

$$V_{Post\ HIP} = V_{As-Cast}[1 - (0.304 - 0.099)] = 2.044 \cdot 10^{-6} m^3 \quad (10)$$

According to the image analysis, the average porosity of the HIPed samples was 0.099%. Therefore, the combined volume of porosity can be obtained by Equation (11)

$$V_{Porosity} = V_{Post\ HIP} \cdot Average_{Porosity\ \%} = 2.044 \cdot 10^{-6} m^3 \cdot 0.099\% = 2.026 \cdot 10^{-9} m^3 \quad (11)$$

The number of pores in the sample can be estimated using Equation (12).

$$Number\ of\ Pores = \frac{V_{Porosity}}{V_{Pore}} = \frac{2.026 \cdot 10^{-9} m^3}{1.8 \cdot 10^{-15}} = 1.15 \cdot 10^6 \quad (12)$$

By multiplying the amount of work required to close a single spherical pore with a diameter of 15 μm (Equation (8) by the total number of pores in the sample, the total work required to close all of the pores is calculated in Equation (13) below.

$$Total\ Work = 3.82\ x\ 10^{-9} KJ \cdot 1.15 \cdot 10^6 = 4.4 \cdot 10^{-3}\ KJ \quad (13)$$

$$\text{And } \frac{Total\ Work}{mass} = 2.5 \cdot 10^{-1}\ \frac{KJ}{kg}$$

Although, 4.4 joules or 4.4 watts per second could not even power a household LED light bulb, the calculation of work is based on volume change. Since there was very little volume change in the sample after HIP'ing, which is a touted benefit of the HIP process, the total work done on the sample was very small due to mechanical work.

3.2 HIP Pressure Required for Pore Closure

In this section, the pressure needed to close a single pore is calculated based on the surface energy of the pore. Then, this value is multiplied by the total number of pores in the sample calculated in Equation (12). To perform these calculations, the following assumptions are needed:

- The pore diameters are 15 um based on the average pore size measured in the as-cast sample
- The shear modulus of CM247 at 950^{o}C = 60 Gpa (Rajendran, Petley, & Rehmer, 2012)
- The lattice parameter of the most abundant phase, gamma prime, is a_o= 0.359 nm (Singh, 2011)

First, the magnitude of the burgers vector is calculated. For an FCC material the shortest distance to slip during deformation is from the cube corner to a face centered position as pictured in Figure 16.

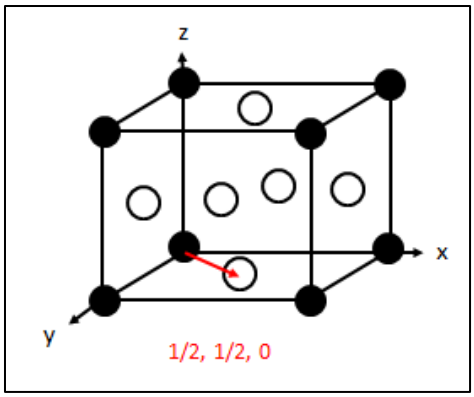

Figure 16: Shortest slip distance in an FCC material

The burgers vector can then be written as $\frac{a_o}{2}[1,1,0]$ and the magnitude for this burgers vector can be calculated using Equation (14) below from (Smallman & Ngan, 2007).

$$|b| = a_o\sqrt{u^2 + v^2 + w^2} = 0.359\sqrt{(\frac{1}{2})^2 + (\frac{1}{2})^2 + 0^2} = 0.254\,nm \tag{14}$$

Next, the surface energy of a pore, γ_s, can be calculated using the shear modulus, μ, for CM247 at 950^{o}C and the magnitude of the burgers vector, b, in Equation (15) from (Smallman & Ngan, 2007)

$$Surface\ Energy = \gamma_s = \frac{\mu b}{10} \tag{15}$$

$$\gamma_s = \frac{60GPa \cdot 0.254um}{10} = 1.523\ \frac{J}{m^2}$$

With the surface area known, the pressure to close one pore can be calculated using the relationship in Equation (16) from (Smallman & Ngan, 2007):

$$P = \frac{2\gamma_s}{r} \tag{16}$$

$$P = \frac{2\gamma_s}{r} = \frac{2 \cdot 1.523\ \frac{J}{m^2}}{7.5\mu m} = \mathbf{0.406\ MPa}$$

Figure 17 was plotted by artificially choosing a pore diameter and plugging it into Equation (16) above. It can be seen that as pore size decreases, it requires more energy to completely close a pore. This is due to the increasing internal gas pressure as the pore size decreases. This could be the main benefit of HIP'ing at high pressures. The smaller the pore gets, the more external pressure is required to overcome the gas pressure internal to the pore.

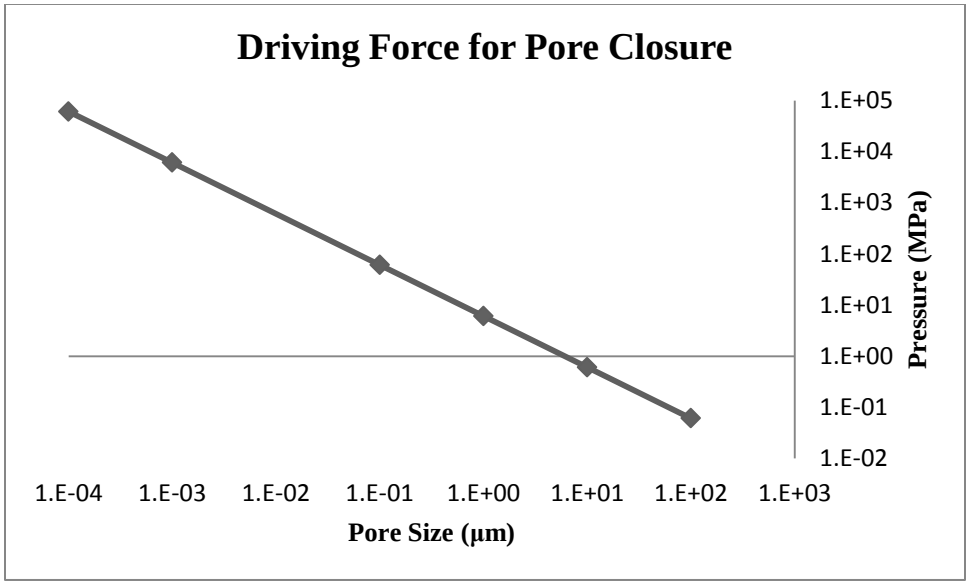

Figure 17: Pore closure requires more energy as the pore size decreases

Figure 18 shows that as the temperature is increased, the pressure required to close a pore decreases. This is due to the temperature dependence of the pore surface energy. As the temperature increases, the shear modulus decreases; thus, the surface energy decreases (Equation 14). Additionally, high temperatures would increase the activity of the gas and surrounding metal which would help diffuse the gas molecules into the metal. If enough time is provided, the gas molecules should escape to the sample surface which would also eliminate the porosity.

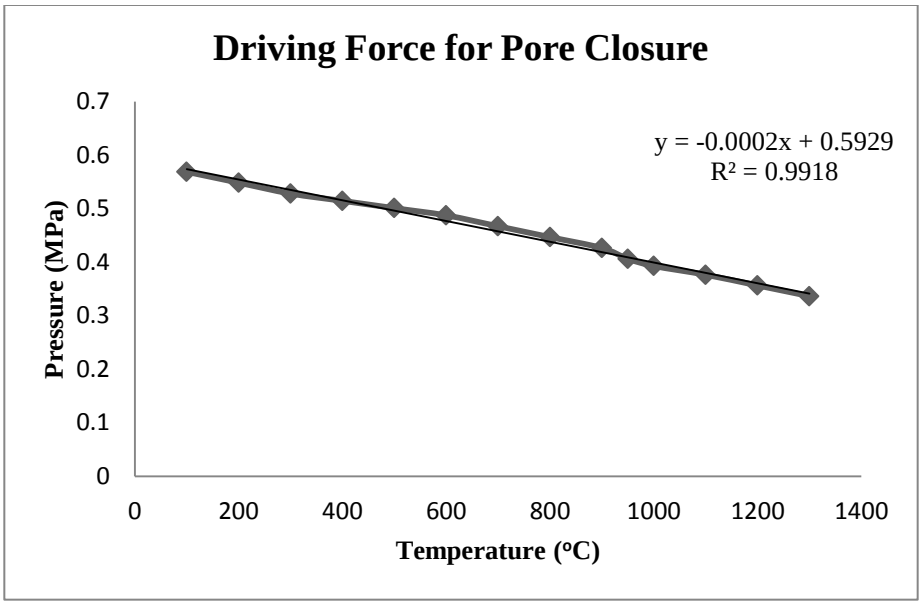

Figure 18: The required pressure to close a pore decreases with increasing temperature (pore diameter = 15 µm)

These calculation show that there are benefits of applying both high temperature and pressure to superalloy castings to eliminate porosity. The next sections calculate the actual energy input into a superalloy casting using typical HIP'ing parameters for CM247.

3.3 Total Energy Input by HIP Process

The first law of thermodynamics was used to estimate the total energy input into a sample of CM247 during a typical HIP cycle for this material. Total energy was estimated in an effort to better understand the influence of temperature and pressure during the HIP process and then compare the findings to the modified HT process. To perform these calculations, the following assumptions are required:

- The as-cast average porosity percent was measured to be 0.304% in the as cast sample
- The as-cast average porosity percent was measured to be 0.099% in the HIP sample

- The average diameter of all the porosity measured in the as cast samples was 15 μm. Therefore, in the calculations, all pores are assumed to have a 15 μm diameter.
- The sample dimensions were = 0.013 m x 0.025 m x 0.006 m which results in a volume, V, of 2.048 x 10^{-6}
- The density, ρ, of CM247 LC is $8.50\frac{g}{cm^3}$ (Harris, K; Erickson, G L; Schwer, R E;, 1984)
- Room temperature, $T_1, = 20°C$
- HIP processing temperature, $T_2, = 1185°C$
- HIP processing pressure, $P, = 173\ MPa$
- Specific heat, C, was extrapolated using research data plotted of Mar-M-247, a predecessor to CM247, is $0.60\frac{J}{g \cdot K}$ (Przeliorz, Binczyk, Gradon, Goral, & Mikuszewski, 2014)

The sample mass can be calculated using Equation (17) below.

$$\text{Sample mass} = \rho * V = 0.017\ kg \tag{17}$$

Equation (18) is the First Law of Thermodynamics and is used to determine the total amount of energy input into the sample of CM247 during the HIP cycle.

$$E_{energy\_total} = Q_{heat\_in} + W_{work\_in} \tag{18}$$

The heat energy input into the sample can be calculated using Equation (19) below:

$$Q_{heat_{in}} = mass \cdot C \cdot \Delta T \tag{19}$$

Plugging in mass, specific heat and the change in temperature during the HIP cycle yields:

$$Q_{heat_{in}} = 0.017\ kg \cdot 0.58\frac{J}{g \cdot K} \cdot 10^3 \cdot 273.15 \cdot (1185℃ - 20℃) = 3.41 \cdot 10^3\ KJ$$

$$\text{And } \frac{Q_{heat_{in}}}{mass} = 1.96 \cdot 10^5 \ \frac{KJ}{kg}$$

The work energy input into the sample can be calculated using Equation (20) below:

$$W_{in} = \int_{V_1}^{V_2} P \cdot dV \tag{20}$$

Integrating and plugging in pressure and volume change of the sample during the HIP cycle yields:

$$W_{work_{in}} = 173 \cdot 10^6 \cdot (V1 \ - V2) = \frac{0.775\ J}{1000} = \ 7.25 \cdot 10^{-4}\ KJ$$

$$\text{And } \frac{W_{work_{in}}}{mass} = 4.16 \cdot 10^{-2} \ \frac{KJ}{kg}$$

Adding the results from Equations (19) and (20) gives the total energy input into the sample during the HIP cycle.

$$E_{energy\_total} \ = 3.41 \cdot 10^3\ KJ + \ 7.25 \cdot 10^{-4}\ KJ = \ 3.41 \cdot 10^3\ KJ$$

$$\text{And } \frac{E_{energy\_total}}{mass} = 1.96 \cdot 10^5 \ \frac{KJ}{kg}$$

Based on these calculations, most of the energy input during the HIP cycle is in the form of heat energy. This observation is in agreement to the findings in section 3.1. Due to the lack of a significant volume change during the HIP cycle, the calculated work will be low. Conversely, the temperature delta incurred by the cast superalloy during the HIP cycle is large; therefore, the thermal energy is calculated to be a large amount.

CHAPTER 4. EXPERIMENAL PROCEDURE

4.1 Casting of Alloy CM247

The CM247 samples used in this study were taken from a slab poured during a production run. The raw material was melted using a vacuum induction furnace. After the investment cast molds were filled, remaining liquid metal was poured into a rectangular slab as seen in Figure 19. The process VIM and investment casing were described in section 2.2.2.

Figure 19: As cast slab of CM247

4.2 Hot Isostatic Pressing and Heat Treatment

Samples were sectioned from the slab of CM247 using a wet metallographic cut off saw similar in design to the saw pictured in Figure 20. The saw uses liquid cooling medial and a slow grinding wheel rpm to ensure the material being machined does not experience any microstructural changes during machining.

Figure 20: Example of a wet abrasive cut-off saw (MAGER, 2015)

After sectioning samples from the original slab, two samples were sent to a manufacturer for HIP and solution heat treatment. The manufacturer put both samples into a production batch for the HIP cycle with similar parameters as reported by (Huang & Koo, 2004) which were 1185ºC/173MPa/4hrs. Figure 21 shows a schematic of a typical HIP furnace. Inside the furnace, the workpiece is heated and subjected to an inert gas at high pressure, usually argon.

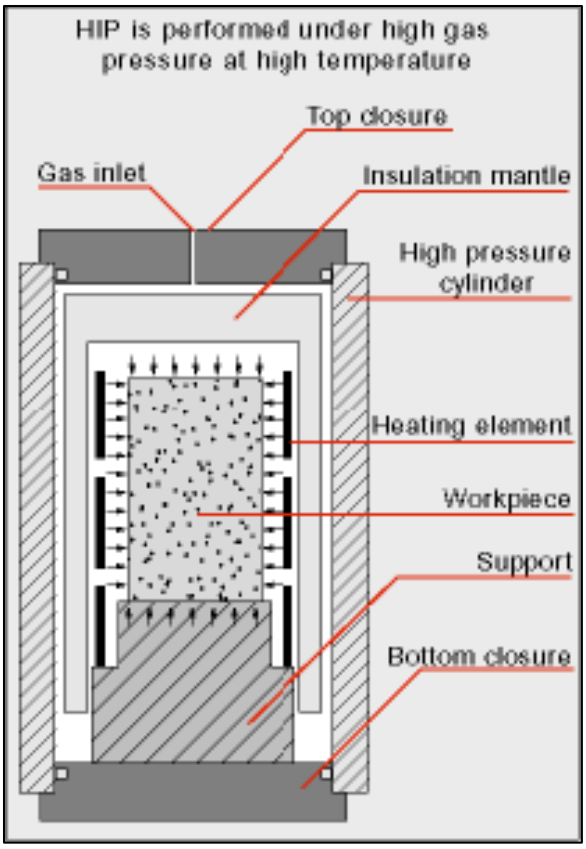

Figure 21: Example of a HIP furnace (EVERLOY, 2005)

After HIP'ing, one of those samples was then included into a solution heat treatment production cycle with similar parameters, 1232ºC/2hrs, as reported by (Huang & Koo, 2004).

Next, six samples were removed from the as-cast slab. These samples were encapsulated into argon purged glass tubes as seen in Figure 22.

Figure 22: Typical image of one of the six as-cast samples that were encapsulated in glass tubes

The six samples were then subjected to six different heat treatment cycles outlined in Figure 23 and Figure 24 using a CM 1710 rapid high temperature (1700ºC) furnace with vertical cycling capability pictured in Figure 25 and Figure 26.

.

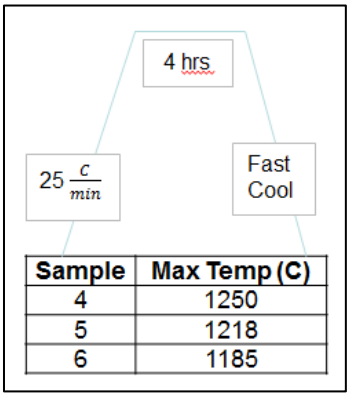

Sample	Max Temp (C)
4	1250
5	1218
6	1185

Figure 23: Ramp rate and hold time for modified HT # 1

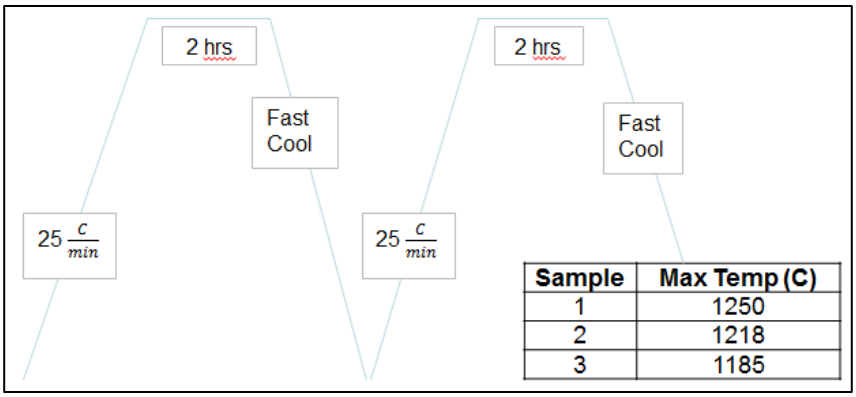

Sample	Max Temp (C)
1	1250
2	1218
3	1185

Figure 24: Ramp rate and hold time for modified HT # 2

Figure 25: CM 1710 rapid high temperature (1700ºC) furnace with vertical cycling capability

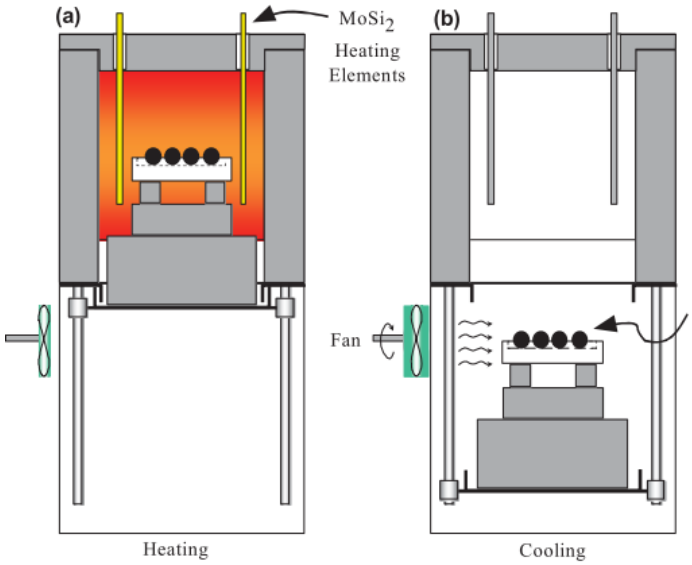

Figure 26: Schematic of CM 1710 rapid high temperature (1700°C) furnace with vertical cycling capability (Liu, 2007)

Following all the processing steps, nine samples were available for microscopy analysis. Three samples were used, one from each of the standard production processing steps; initial casting, HIP and solution heat treatment. Six samples were developed using six different modified heat treatments in place of the standard production processes. The differentiation is displayed in Figure 27.

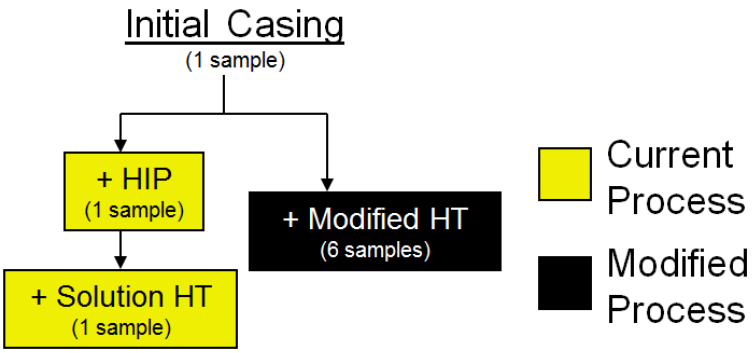

Figure 27: Sample process differentiation

4.3 Microstructural Characterization & Quantitative Analysis

Nine samples were analyzed: each undergoing the processing steps documented in Table 1 below.

Table 1: Sample configurations

Sample #	Analyzed Configuration
1	As-Cast
2	As-Cast + HIP
3	As-Cast + HIP + Solution Heat Treat
4	As-Cast + Modified HT (4 hours @ 1250º C)
5	As-Cast + Modified HT (4 hours @ 1218º C)
6	As-Cast + Modified HT (4 hours @ 1185º C)
7	As-Cast + Modified HT (2 x 2 hours @ 1250º C)
8	As-Cast + Modified HT (2 x 2 hours @ 1218º C)
9	As-Cast + Modified HT (2 x 2 hours @ 1185º C)

After thermal processing, the samples were mounted into polymer potting material using a mounting press similar to the one pictured in Figure 28.

Figure 28: Metallurgical sample mounting press (Allied, 2015)

Each sample is individually placed inside the pressing chamber, and then the chamber is filled with potting material. The chamber lib is closed and the machine melts the potting material and presses the sample and potting material into a compact cylindrical shape. The sample remains at the bottom of the cylinder so less work is required to expose the metal during polishing. Typical samples are displayed in in Figure 29, Figure 30 and Figure 31.

Figure 29: Mounted as cast sample prior to polishing

Figure 30: Mounted Cast + HIP sample prior to polishing

Figure 31: Mounted Cast + HIP + Solution Heat Treated sample prior to polishing

After the samples were mounted, they were polished to prepare them for study of porosity. The samples were placed into the Zeiss Ultra-55 FEG scanning electron microscope (SEM) and backscatter electron scanning images were taken from the nine samples. Each sample had at least eleven backscatter images captured for microporosity analysis. The porosity percent from each image was analyzed using Leica-Microsystem's LAS Image Analysis software. By first calibrating the pixel vs. micrometers and the image contrast, the image analysis software accurately calculated the porosity percentage observed in the sample. A typical backscatter image post image analysis is shown in Figure 32.

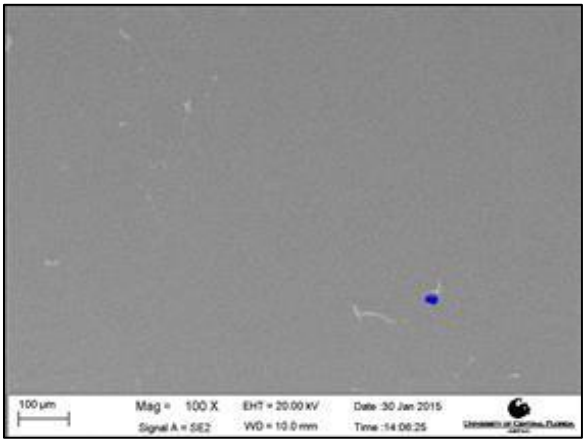

Figure 32: Typical backscatter image of the as-cast sample with porosity captured using the Leica software

Next, the samples were etched using Glyceregia and images were captured using the SEM to analyze the gamma prime phase in each sample. Acid etching removes the gamma prime phase on the surface of the sample, resulting a darker appearance compared to the gamma matrix. The image analysis software used this contrast between the gamma and gamma prime phase to calculate the gamma prime volume fraction, size and shape.

A typical etched SEM image can be seen in Figure 33. The gamma prime phase appears uniform and medium sized in this image. The darker areas in the image are the gamma prime phase particles while the lighter areas in between is the gamma, matrix phase.

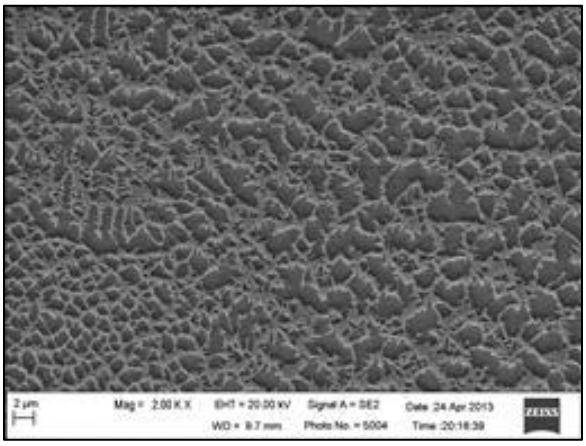

Figure 33: SEM image of polished and etched As-Cast sample

Figure 34 displays the post processed image where the colors are the gamma prime phase surrounded by the gray gamma matrix. Each color represents similarly sized areas for visual recognition. The statistical data output form the LAS software was stored and analyzed.

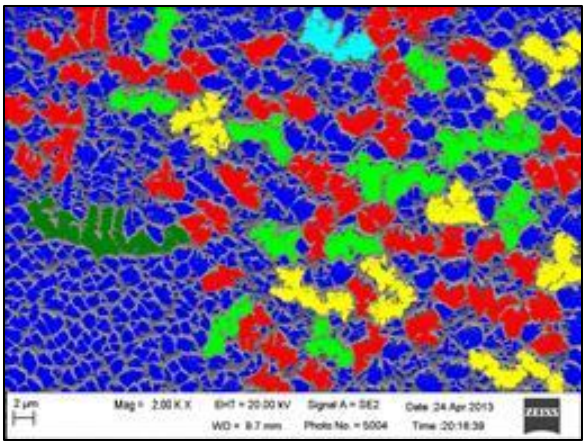

Figure 34: Post processed image of polished and etched As-Cast sample

CHAPTER 5. POROSITY AND GAMMA-PRIME PHASE ANALYSIS OF CM247

5.1 CM247 Produced by Conventional HIP and Solution Heat Treatment

Samples one, two and three were produced according to standard production parameters. The cast sample was removed from the original slab and analyzed in the as-cast state. The HIP and solution heat treatment samples were sent to a company that placed the samples in with production batches. The HIP cycle and solution heat treatment were performed at similar parameters as reported by (Huang & Koo, 2004) which were 1185ºC/173MPa/4hrs and 1220ºC /2hrs respectively.

5.1.1 Porosity

Samples one, two and three were polished and examined for porosity using an SEM. As expected sample one, the as cast sample, contained the most porosity as observed in Figure 35. Internal porosity is common in superalloy castings, but it should be noted that the total porosity percent presented here was low compared to other superalloy castings. For example, one paper stated that typical porosity percent observed in IN-713C castings were 0.6% - 1.7% (Antony & Radavich, 1980). The average porosity percent of as-cast CM247 studied in this sample was approximately 0.3%. It appears that the modern alloy design, melting process and casting process produces significantly less internal porosity than in years past.

In this study, HIP'ing reduced the porosity by 67.4% compared to the as-cast sample and the solution heat treatment reduced the porosity by another 22.8% compared to the as-cast sample. The total porosity reduction from the as-cast sample to the HIP plus solution heat treatment

sample, using the standard processing parameters, was 90.2%. The standard deviation of the porosity percent was lowest for the as-cast sample at 0.00025 while the solution heat treatment had the second lowest standard deviation of 0.0007. The HIP treatment increased the standard deviation of the porosity percent to a value of 0.0013. This was unexpected because other research suggests HIP'ing reducing material property scatter such as creep life (Lamberigts, Diderrich, Coutsouradis, De Lamotte, Drapier, & Deridder, 1980). However, this may just show that the casting process is well controlled. Estimation of mechanical properties can be linked to porosity but due to the small sample size and complex interaction between microstructure and mechanical properties, estimations cannot be made here.

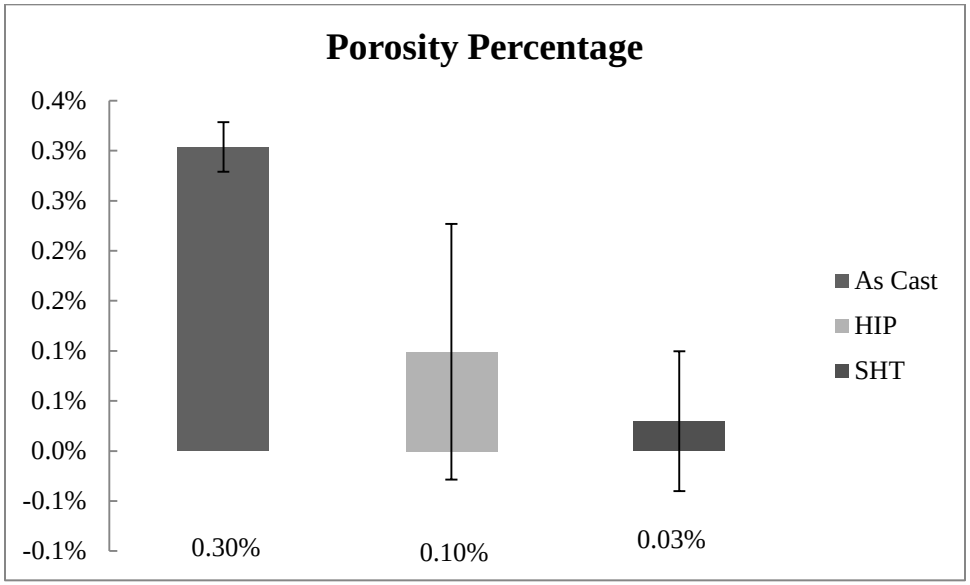

Figure 35: Porosity percent of samples 1 – 3

The figures below show typical images taken from each process step. A small amount of porosity is visible in Figure 36. Typically, internal porosity can be found at interdendritic areas where freezing takes place last. The thought is that these areas can get confined such that liquid metal

cannot fill in the volume due to tortuous pathways or trapped gas pressure. If this occurs, a volumetric defect such as a pore can form.

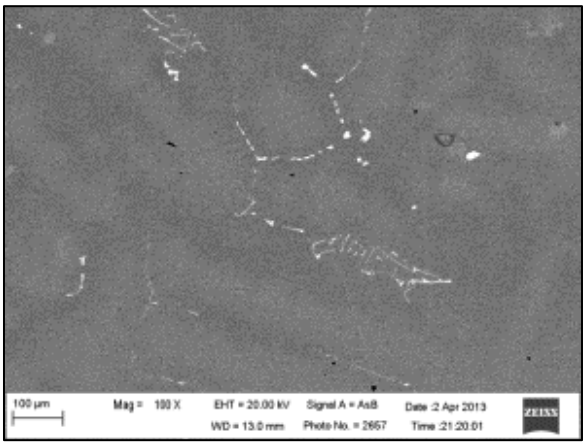

Figure 36: Sample 1, as cast porosity sample

Internal porosity is not easily observed in the HIP sample pictured in Figure 37. Most of the internal porosity was eliminated by the application of high temperature and high pressure argon gas during the HIP treatment.

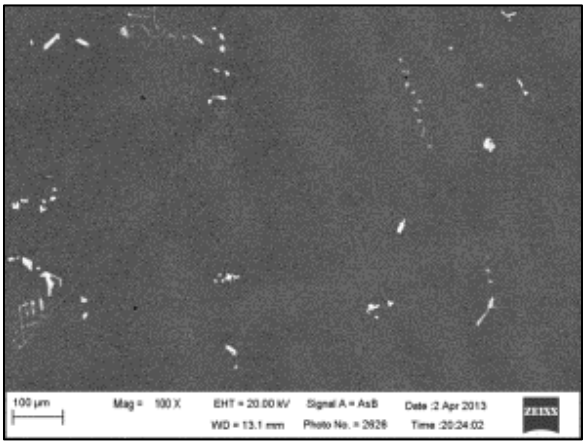

Figure 37: Sample 2, HIP porosity sample

Again, internal porosity is not readily observed in the solution heat treatment sample pictured in Figure 38. All significant internal porosity was eliminated. As with the previous two images, the

carbide phases appear white in the back scatter image captured by the SEM. These particles appear to be MC or $M_{23}C_6$ carbides.

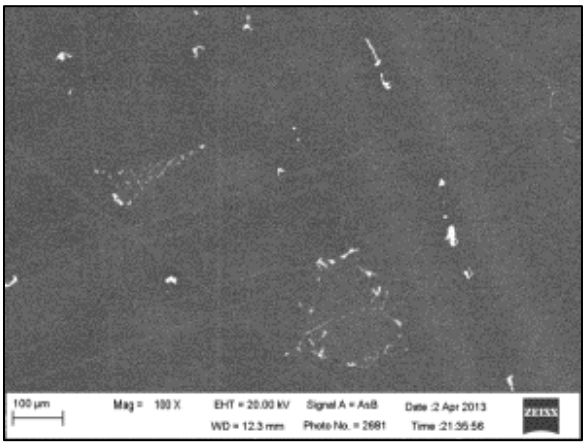

Figure 38: Sample 3, solution heat treatment porosity sample

5.1.2 Gamma Prime Phase

Next, the samples were acid etched using Glyceregia to remove the gamma prime phase on the surface of the sample. This was done to create contrast between the gamma phase and the precipitate gamma prime phase. The contrast can be exploited by image processing software to perform statistical analysis of the images. The volume fraction, ratio between the gamma and gamma prime phase, was calculated using Leica-Microsystem's LAS Image Analysis Software. Figure 39 shows the volume fraction of the gamma prime phase compared to the gamma matrix. According to the literature, high gamma prime volume fraction correlates well with desirable high temperature performance (Sims, Stoloff, & Hagel, 1987).

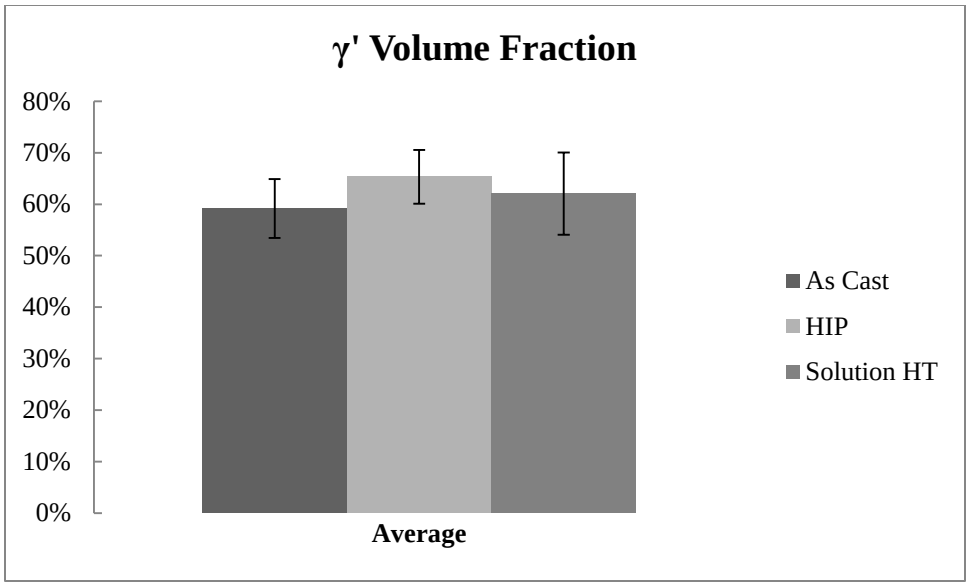

Figure 39: Gamma prime volume fraction for samples 1 through 3

Using the same LAS software, the gamma prime average size was analyzed and plotted as shown in Figure 40. These results show that during the HIP cycle, the gamma prime phase coarsens due to the long hold time at a high temperature. But once solutionized, the gamma prime particles precipitate and form smaller sized particles. Typically, further aging heat treatments would ensure the gamma prime phase is well developed for operation but this thesis does not include a study of the aging heat treatments.

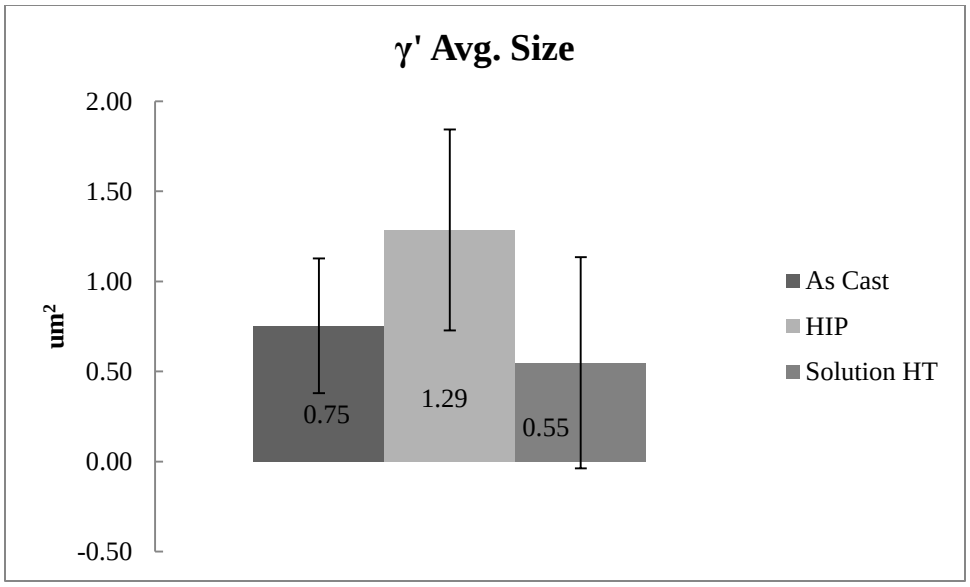

Figure 40: Average size of the gamma prime phase in samples 1 through 3

The figures below show typical images taken from each process step. The image in Figure 41 shows a good example of a uniform medium sized gamma prime phase. The darker areas in the image are the gamma prime phase particles while the lighter areas in between is the gamma, matrix phase.

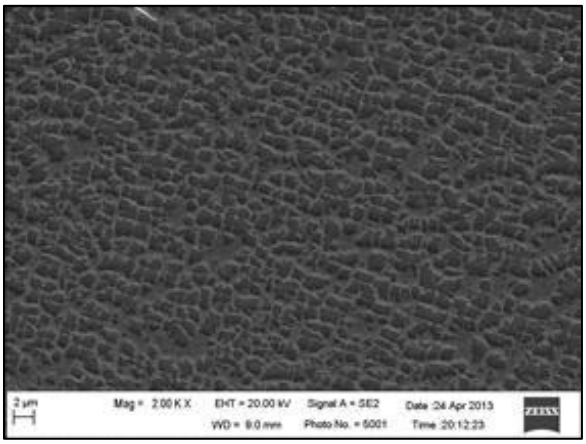

Figure 41: Sample 1, as cast gamma prime phase

The image in Figure 42 shows a non-uniform and enlarged gamma prime phase due to the high temperature applied during the HIP treatment.

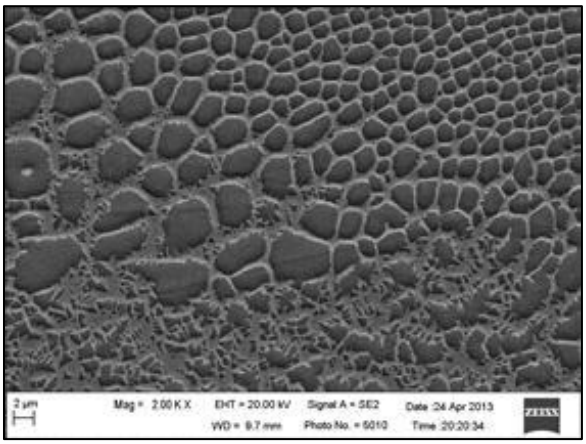

Figure 42: Sample 2, post HIP gamma prime phase

The image in Figure 43 shows a uniform and fine gamma prime phase after the solution heat treatment. This is because the solution heat treatment temperature is high enough to dissolve the gamma prime phase. Upon cooling, the gamma prime particle precipitate out of the gamma matrix and because the cooling rate is fast, the gamma prime particles form small, uniform clusters.

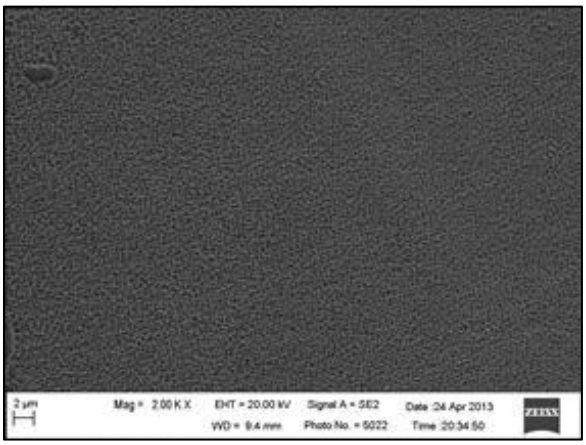

Figure 43: Sample 3, post solution heat treat gamma prime phase

5.2 CM247 Produced by Proposed Heat Treatments without Applied Pressure

Samples four through nine were produced using different heat treatments. The samples were originally obtained from the cast slab of CM247. Samples four through six used a 4 hour heat treatment at 1250ºC, 1218ºC and 1185ºC respectively. Samples seven through nine used a 2 x 2 hour heat treatment at 1250ºC, 1218ºC and 1185ºC respectively.

5.2.1 Porosity

Samples four, five and six were heat treated using the ramp rate, time and temperatures listed in Figure 23. Following thermal processing, the samples were polished and examined for porosity using the SEM. The sample heat treated at 1218 ºC for 4 hours had the lowest porosity percent and the lowest standard deviation of pore size. Conversely, the sample processed at 1185 ºC for 4 hours, had the most porosity compared to the other two samples. This sample also had the highest standard deviation in pore size. The samples processed at 1185 ºC for 4 hours showed a wide range of pore sizes. These results are presented in Figure 44

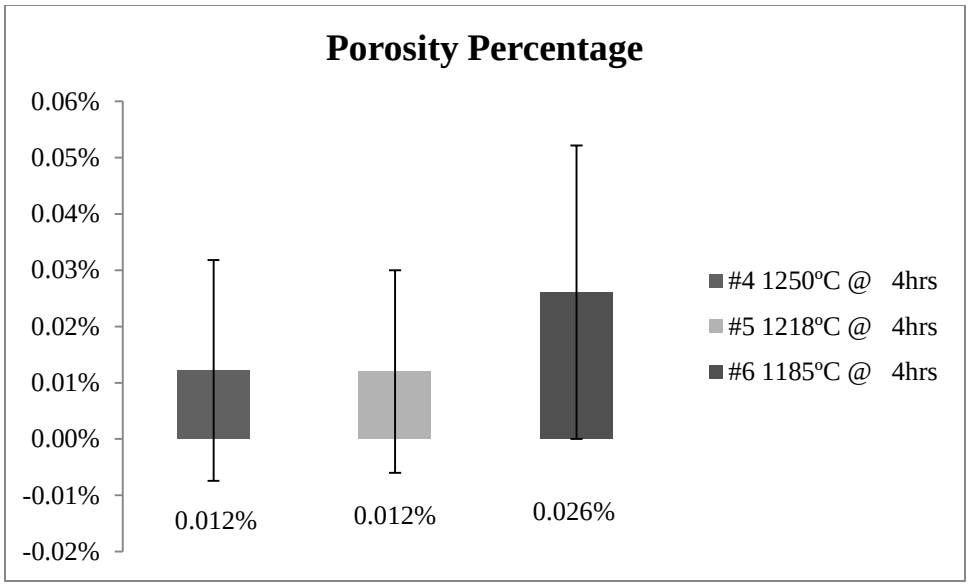

Figure 44: Average porosity percent for the modified heat treat #1

The figures below show typical images taken from each process step. Virtually no porosity was observed in the sample heat treated at 1250ºC for 4 hours. Figure 45 displays a typical image take from the sample. Notice, the carbide phases appear to be similar in quantity compared to the standard production processes described in section 5.1. These particles also appear to be MC or $M_{23}C_6$ carbides.

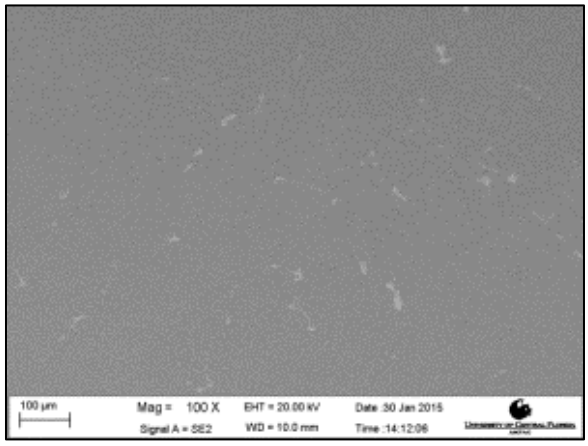

Figure 45: Sample 4, 4 hours @ 1250ºC porosity sample

While the average porosity percent calculated from images take of the sample heat treated at 1218ºC for 4 hours was low, Figure 46 shows an apparent pore in the middle, top of the image. On average this sample had the lowest amount of porosity compared to the other samples heat treated for 4 hours.

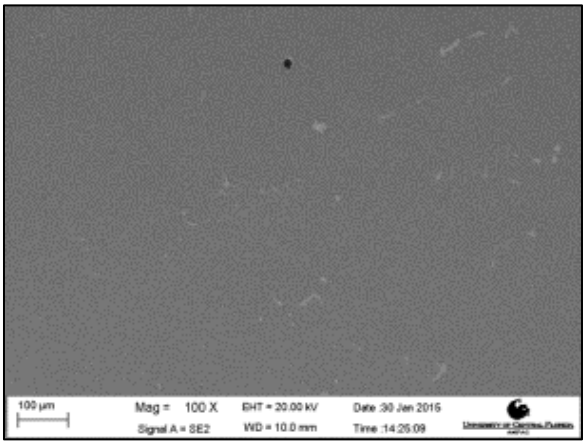

Figure 46: Sample 5, 4 hours @ 1218ºC porosity sample

Figure 47 shows an image take from the sample heat treated at 1185 ºC for 4 hours. This sample had the most porosity compared to the other two samples heat treated for 4 hours. This sample also had the highest standard deviation in pore size compared to the other two samples heat treated for 4 hours.

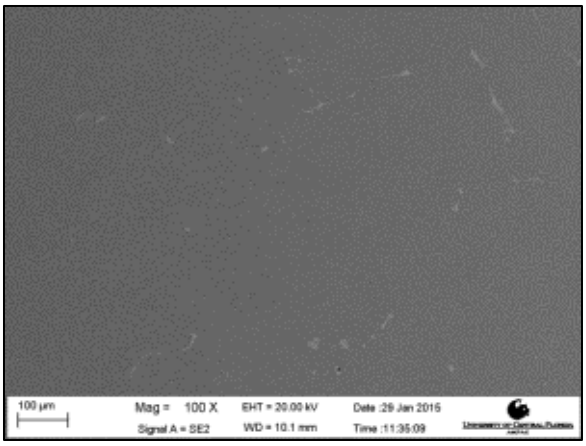

Figure 47: Sample 6, 4 hours @ 1185ºC porosity sample

Samples seven, eight and nine were heat treated using the ramp rate, time and temperatures listed in Figure 24. Follow thermal processing, the samples were polished and examined for porosity using the SEM as presented in Figure 48. The sample heat treated at 1218 ºC for 2 x 2 hours had the lowest porosity percent compared to the other two samples heat treated for 2 x 2 hours. The sample heat treated at 1185 ºC had the lowest standard deviation of pore size compared to the other two samples heat treated for 2 x 2 hours. The sample processed at 1250 ºC had the most porosity and the highest standard deviation in pore size compared to the other two samples heat treated for 2 x 2 hours.

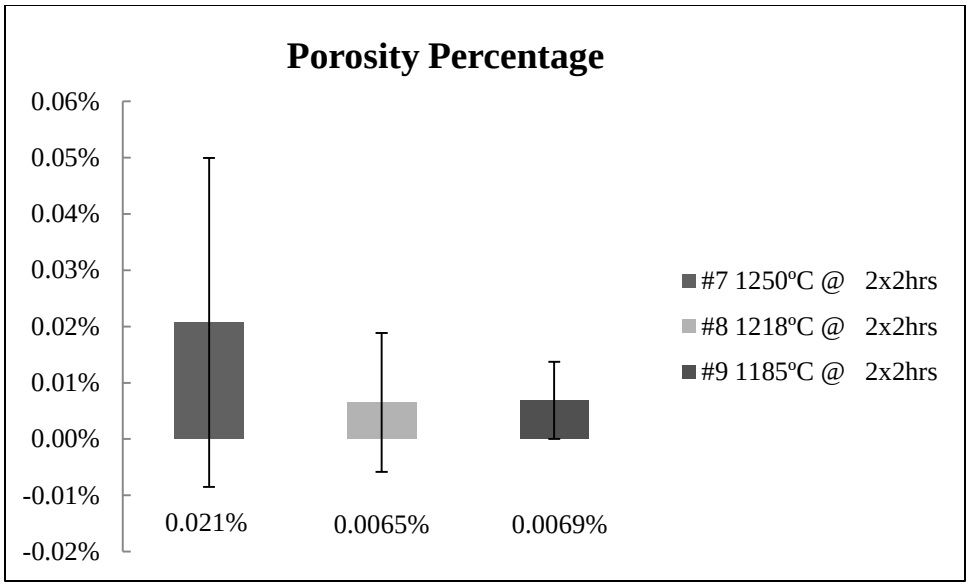

Figure 48: Average porosity percent for the modified heat treat #2

The figures below show typical images taken from each process step. Figure 49 shows an image taken from the sample heat treated at 1250 ºC for 2 x 2 hours. This sample was processed at the highest temperature which appears to be the least productive for removing porosity.

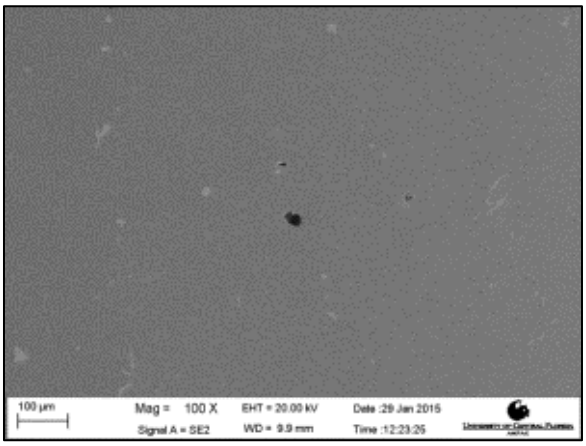

Figure 49: Sample 7, 2x2 hours @ 1250 ºC porosity sample

Figure 50 shows an image taken from the sample heat treated at 1218 ºC for 2 x 2 hours. This sample had virtually all internal porosity removed and had the second highest standard deviation of pore size.

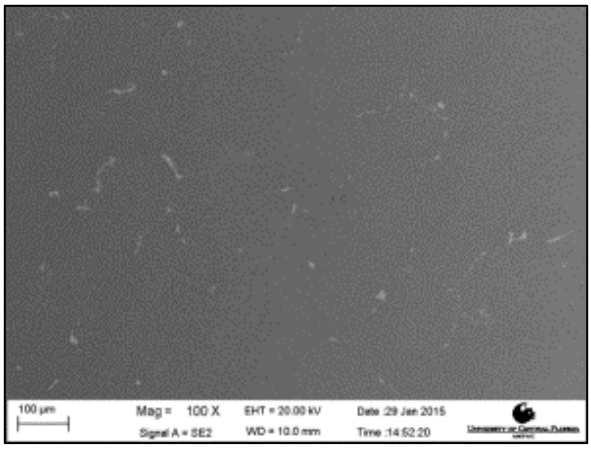

Figure 50: Sample 8, 2x2 hours @ 1218 ºC porosity sample

Figure 51 shows an image taken from the sample heat treated at 1185 ºC for 2 x 2 hours. This sample had a similar amount of porosity as the sample treated at 1218 ºC for 2 x 2 hours, albeit, slightly more. However, standard deviation of pore size was the lowest for this sample.

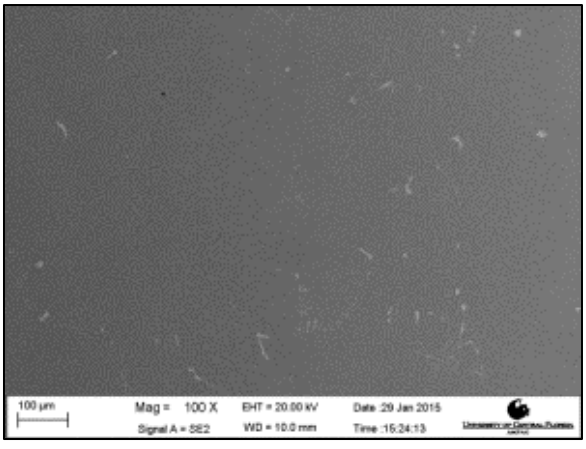

Figure 51: Sample 9, 2x2 hours @ 1185 ºC porosity sample

5.2.2 Gamma Prime Phase

Similar to the steps taken for samples one, two and three, samples four through nine were acid etched using Glyceregia to remove the gamma prime phase on the surface of the sample. The volume fraction was calculated using images taken from each sample using Leica-Microsystem's LAS Image Analysis Software. Figure 52 shows the volume fraction of the gamma prime phase compared to the gamma matrix for samples four through nine.

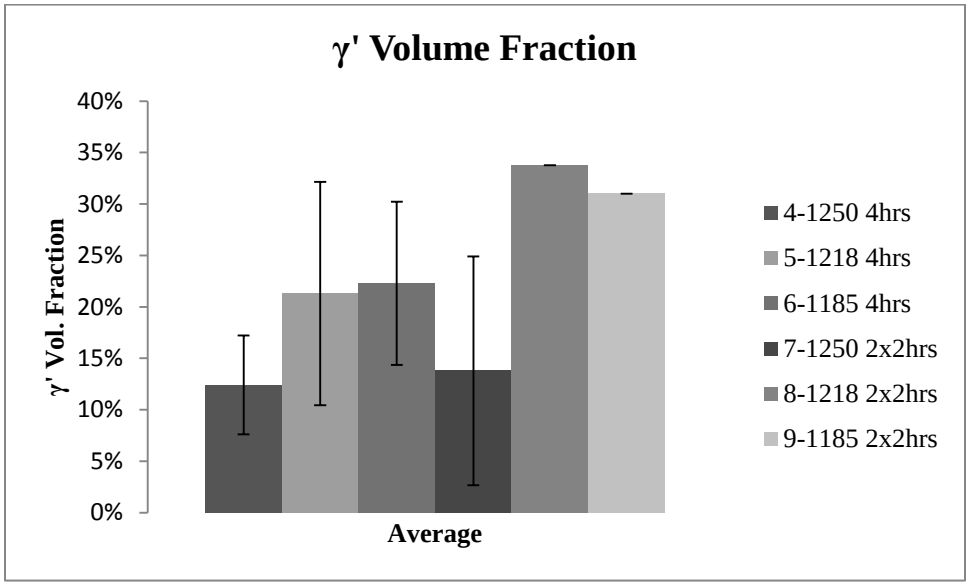

Figure 52: Gamma prime volume fraction for samples 4 through 9

Samples eight and nine had the most amount of gamma prime phase respectively. However, only one image was analyzed for each of these samples whereas, ten or more images were captured for the other samples. Further, there was one image in samples five and six that had similar volume fraction results as the one image take from each sample eight and sample nine. Therefore, due to lack of statistical data available, it cannot be determined if the 2 x 2 hour heat treatment would always result in more of the gamma prime phase present compared to the 4

hours long heat treatment. Clearly, the higher temperature processes resulted in less gamma prime present in samples four and seven compared to the other samples. This is likely because the high temperature thermal treatment induced more energy which dissolved most of the gamma prime phase.

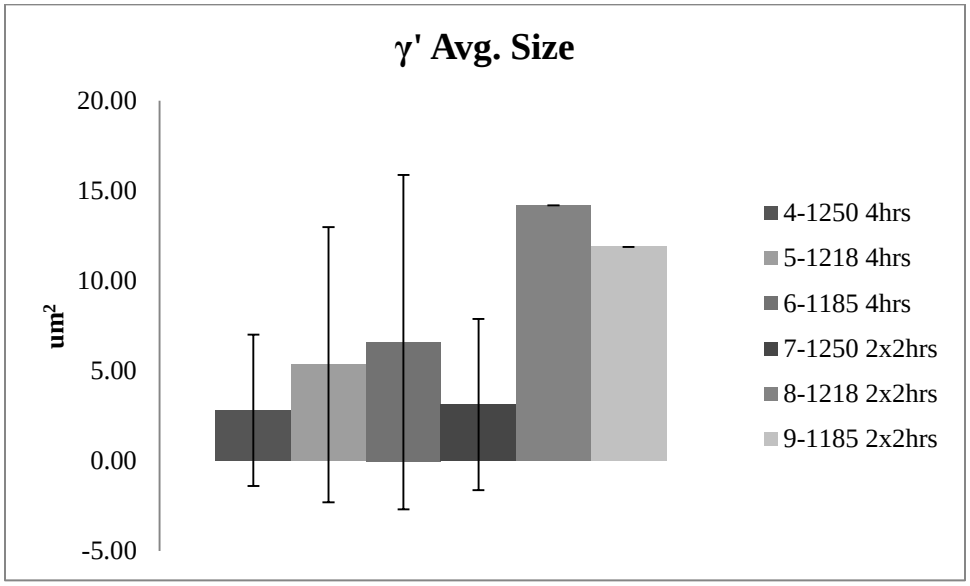

Figure 53: Average size of the gamma prime phase in samples 4 through 9

Similarly, the average size of the gamma prime particles where larger for samples eight and nine. However, only one image was analyzed for each of these samples whereas, ten or more images were captured for the other samples. Further, all but sample four had one image with a similar average size of gamma prime particles as in samples eight and nine. Therefore, due to lack of statistical data available, it cannot be determined if the 2 x 2 hour heat treatment would always result in larger average gamma prime particle size compared to the 4 hours long heat treatment. Clearly, the higher temperature processes resulted in smaller average sized gamma prime particles present in samples four and seven. Combining this result with the low gamma prime volume fraction of the higher temperature samples shown in Figure 52, it is evident that the high

temperature thermal treatment caused the gamma prime phase to dissolve in in the matrix. Due to the rapid cool down, only a limited number of fine gamma prime particles were able to precipitate during cooling.

5.3 Combined Data

The average porosity percent for all the samples are combined on one graph below for comparison as presented in Figure 54, Figure 55 and Figure 56. The combined plot in Figure 54 clearly shows that the modified heat treatments reduced porosity better than the standard production process. The samples that received the 2 x 2 hour modified heat treatments at 1218 ºC and 1185 ºC had the lowest and second lowest porosity percent compared to all the samples. The average porosity from the samples heat treated at 1218 ºC in the modified process #2 was 7.7% lower than the average porosity in the samples processed the current, standard way. The standard deviation in the pore sizes was also much less for the modified heat treatment samples compared to the samples processed using the standard techniques. The HIP plus solution heat treatment reduced the porosity by 90.2 % from the as-cast but the 1218 ºC sample from the modified process #2 batch reduced porosity by 97.9%.

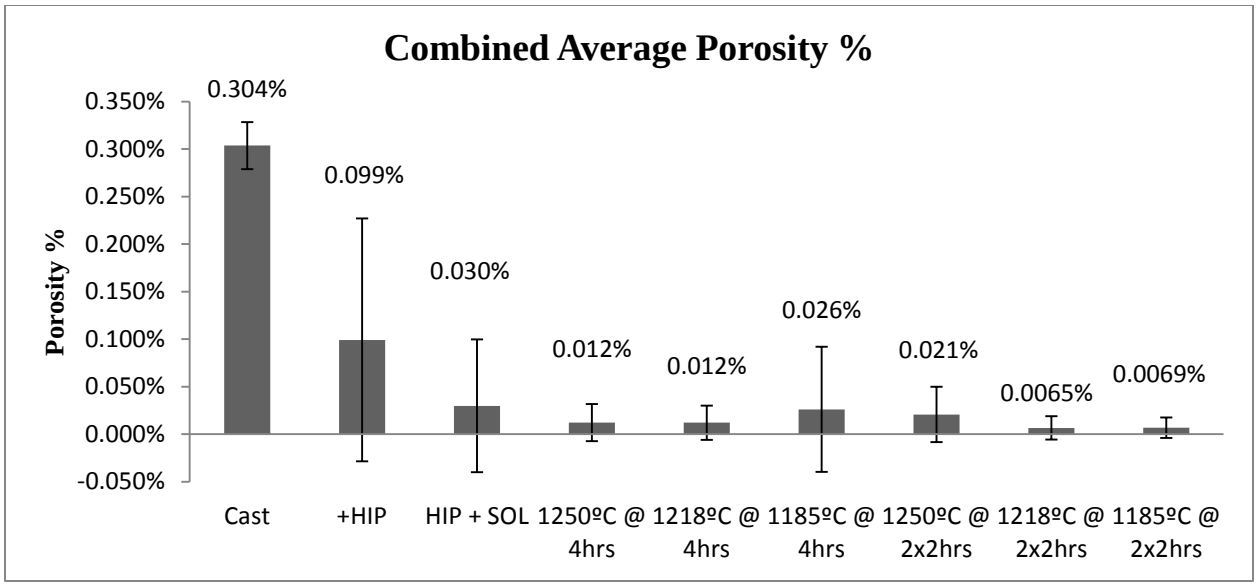

Figure 54: Combined porosity data

The combined plot in Figure 55 displays the average measured gamma prime volume fraction. There is a marked drop in volume fraction after the modified heat treatments were performed. This is an undesirable result. The sample heat treated at 1218 ºC for 2 x 2 hours displays the most gamma prime phase after the heat treatment but the volume fraction is still almost half as much as the standard process.

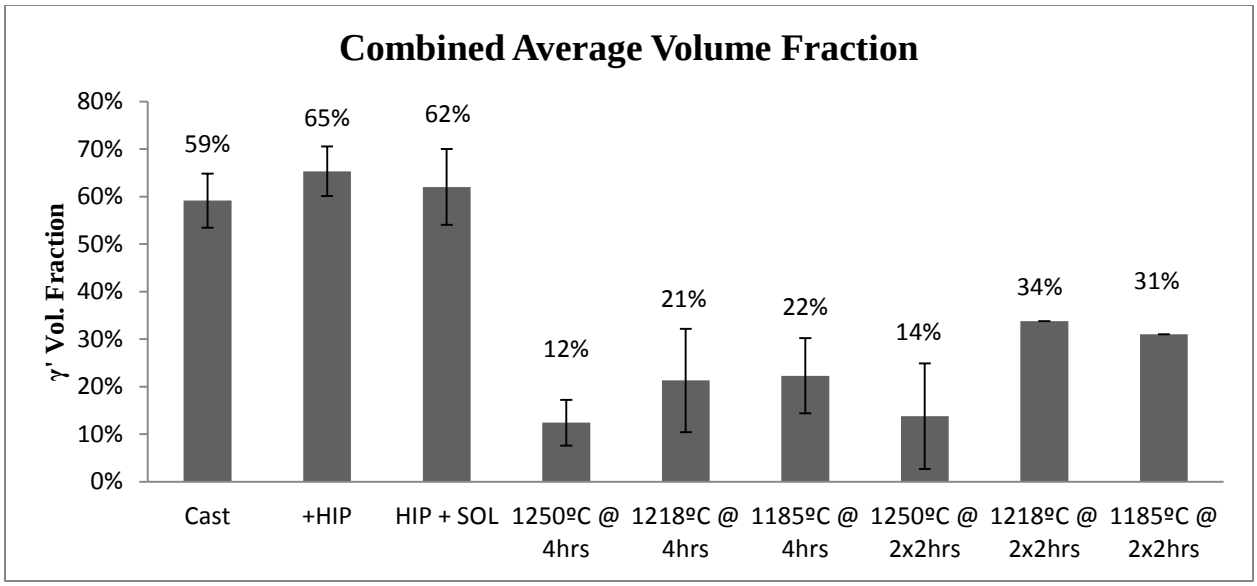

Figure 55: Combined average gamma prime volume fraction data

The combined plot in Figure 56 displays the average measured gamma prime size. The gamma prime particles in the sample which experienced a modified heat treatment were much larger than the particle sizes in the current process. This is an undesirable result. The sample heat treated at 1250 ºC for 4 hours displays the smallest gamma prime phase size but the particle size is still more than double the average particle size of observed in the standard process samples.

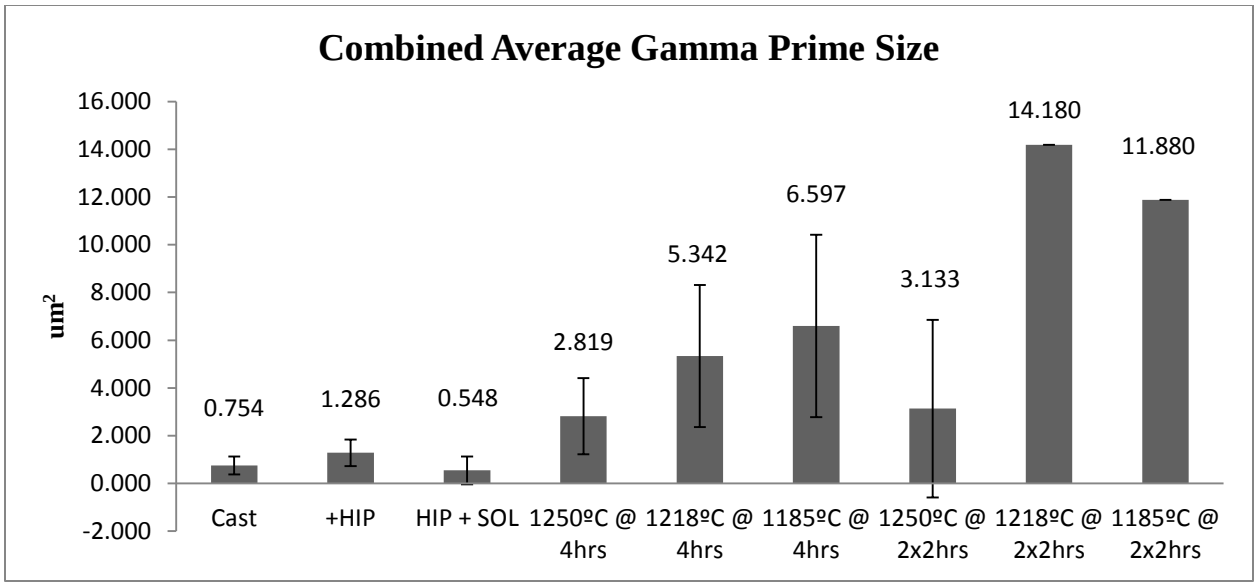

Figure 56: Combined average gamma prime size data

CHAPTER 6. DISCUSSION

This thesis focused on eliminating internal casting porosity in CM247. Currently, the HIP process is used to eliminate porosity in superalloy castings. HIP'ing can only be performed by a limited number of companies which results in long lead time and costly superalloy castings. This study explored alternatives to the HIP process knowing that the current alloy design, melting and casting processes yield relatively low amounts of internal porosity in superalloy castings compared to years past.

Internal pore closure must have an external driving force if pore closure is expected. Calculations were performed, in CHAPTER 3, to explore the impact of the temperature and pressure on internal porosity – the main driving forces for pore closure. These calculations show that the total energy input into the superalloy castings is primarily thermal energy provided during the HIP process. Based on the calculations, HIP pressure has a minimal impact on the total energy input into the superalloy casting because the energy is derived from work. Work requires a volume change and the volume of a pore is so small that the calculated work energy is correspondingly very small or negligible compared to the thermal energy.

Knowing most of the energy input into a superalloy casting during HIP comes from the thermal energy; two different heat treatment cycles were employed. Each heat treatment cycle was performed at three different temperatures, without pressure. The lowest temperature was 1185 ºC. This temperature was chosen because it is the lowest temperature typically used in a standard HIP treatment for this alloy. Next, 1218 ºC was chosen because it is the highest temperature typically used in a standard HIP treatment for this alloy. Finally, 1250 ºC was chosen because it is slightly higher than the typical solution heat treatment temperature for CM247. The gamma

prime phase goes into solution just above this temperature (Yunrang, Luobao, & Chenggong, 1989).

The first approach was to perform a heat treat with the same hold time, 4 hours, as the standard HIP process. The samples heat treated at the highest two temperatures showed the least amount of porosity.

Next, a heat treatment which employed two heating and cooling cycles was used to explore the effects of rapid cooling on internal porosity. It was postulated that two rapid cools would impart more thermal stress on the pore by contracting the outer sample surface relative to the inner sample surface where porosity exists. The thought was that the thermal contraction would impart enough stress to collapse the internal porosity. The two highest temperature samples heat treated for 2 x 2 hours had the least amount of porosity compared to all the samples studied in this research. Both samples had a very similar amount of porosity so it would be recommended to use a 2 x 2 hour heat treatment at 1218 ºC to minimize production cost.

However, the gamma prime volume fraction and average particle size were vastly different for the modified heat treatment samples compared to the samples processed using the standard process (HIP + SOL HT). The general consensus in the literature is that higher volume fractions of gamma prime and evenly dispersed fine particles of gamma prime result in better mechanical properties. The average gamma prime volume fraction and the average gamma prime particle size were negatively impacted by the modified heat treatments. For example, the sample containing the least amount of porosity was heat treated at 1218 ºC for 2 x 2 hours. This sample had 46% less gamma prime phase and the particles that were present were 2486% larger than the HIP + solution heat treatment samples. Figure 57 shows the interaction between dislocations and

gamma prime particle size. The average gamma prime particle size measured in the modified heat treatment samples were all more than 2.8 microns which is off the chart shown in Figure 57. If the gamma prime particles are so few and so large that dislocation can bypass them, the high temperature performance will be degraded.

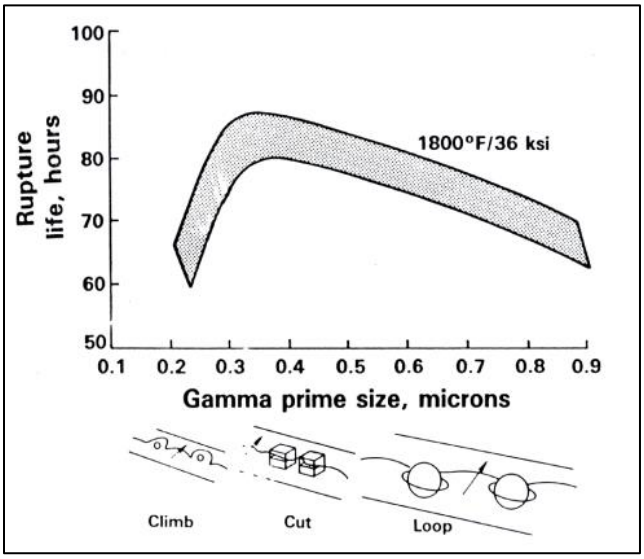

Figure 57: Interaction between dislocation and gamma prime particle size (Boone & Fuchs, 2010)

When a superalloy is heated to very high temperatures, some phases may start melting before other parts of the microstructure. This is called incipient melting and porosity is known to form in these local, melted regions (Tien & Caulfield, 2015). Apparently, due to the significant lack of porosity in the modified heat treatments, it is possible the incipient melting temperature of the gamma prime phase was not reached. Also, it is possible the cooling rate was not optimal during the modified heat treatment allowing the gamma prime phase to significantly coarsen. Alternatively, it is possible that there was not enough time provided during the modified heat treatment, when cooling, to precipitate gamma prime particles. In this case, subsequent age heat treatments may help increase the gamma prime volume fraction.

Based on the results from this study, it is recommended to replace the HIP treatment with a 2 x 2 hour heat treatment at 1218 ºC as a starting point. Then, to optimize the gamma prime phase, perform experiments with the cooling rates and subsequent aging heat treatments to develop a high gamma prime volume fraction alloy with fine gamma prime precipitates.

CHAPTER 7. CONCLUSIONS AND RECOMMENDATIONS

Hot Isostatic pressing greatly increases casting cost and lead times due to a limited number of suppliers that have HIP'ing capabilities. The calculations in CHAPTER 3 show the thermal energy input during the HIP process far exceeds the energy exerted on the casting due to pressure. This is primarily because pressure work requires a volume change and the average porosity percent in the as-cast sample was only 0.3 %. Therefore, with such a low volume of porosity, even if full densification is achieved, the volume reduction is low so the work energy is low.

The results in this study show HIP'ing appears to remove porosity by 67.4% compared to the as-cast sample. Interestingly, the modified heat treatments were able to reduce the average porosity even more. For example, by heat treating a sample at 1218 ºC for 2 x 2 hours, porosity was reduced by 97.9% compared to the as-cast sample. This is a 30.5% decrease in porosity compared to the standard HIP process.

Other factors besides porosity impact alloy performance such as the amount and size of the main strengthening phase, the gamma prime phase. Based on findings in this report, porosity was significantly reduced with the modified heat treatment but the average gamma prime volume fraction was reduced and the average gamma prime particle size was increased compared to the standard HIP process. Decreasing the gamma prime volume fraction and increasing the gamma prime particle size to the extent observed in this study would likely result in undesirable high temperature performance.

Therefore, as a follow on to this study, it is recommended to replace the HIP treatment with a 2 x 2 hour heat treatment at 1218 ºC as a starting point. Then, to optimize the gamma prime phase,

perform experiments with the cooling rates and subsequent aging heat treatments to develop a high gamma prime volume fraction alloy with fine gamma prime precipitates.

APPENDIX A: CALCULATED GAS TURBINE PERFORMANCE DATA

Table 2: Raw data from GAS TURBINE performance calculations

Ideal	36.9%	48.2%	53.9%	57.5%	60.1%	62.2%
PR	Turbine Work					
5	545.5159	560.89	576.264	591.638	607.012	622.386
10	713.393	733.4982	753.6034	773.7086	793.8138	813.9191
15	797.241	819.7093	842.1775	864.6458	887.114	909.5823
20	851.1085	875.0949	899.0813	923.0676	947.054	971.0404
25	889.9466	915.0275	940.1084	965.1893	990.2703	1015.351
30	919.892	945.8168	971.7417	997.6666	1023.591	1049.516
	Compressor Work					
	224.1418	357.3163	448.3585	519.6579	579.142	630.6395
	Heat in					
	854.25	879.375	904.5	929.625	954.75	979.875
PR	Nth					
5	38%	38%	39%	40%	40%	41%
10	42%	43%	44%	45%	46%	47%
15	41%	42%	44%	45%	46%	47%
20	39%	40%	42%	43%	45%	46%
25	36%	38%	40%	42%	43%	45%
30	34%	36%	38%	39%	41%	43%

APPENDIX B: PORE CLOSURE ENERGY CALCULATION DATA

Table 3: Raw data for Figure 17

Pore Diameter (um)	P (Mpa)
100.0	0.06
10.0	0.61
1.0	6.09
0.1	60.92
0.001	6.09E+03
0.0001	6.09E+04

Table 4: Raw data for Figure 18

Temp (C)	Shear Mod (GPa)	surface energy (J/m^2)	P (MPa)
100	84	4.265	0.57
200	81	4.112	0.55
300	78	3.960	0.53
400	76	3.859	0.51
500	74	3.757	0.50
600	72	3.655	0.49
700	69	3.503	0.47
800	66	3.351	0.45
900	63	3.199	0.43
Temp (C)	Shear Mod (GPa)	surface energy (J/m^2)	P (MPa)
950	60	3.046	0.41
1000	Using Equation: y = -0.0002x + 0.5929		0.79
1100			0.75
1200			0.71
1300			0.67

APPENDIX C: DATA FROM STANDARD PROCESS

Table 5: Raw data from gamma prime analysis of standard process

Description	Image	Total Area	Accepted Area	% gamma	% gamma'	gamma' avg size (um^2)	Std Dev
As-Cast							
Pore	200002	343.22	221.77	35%	65%	0.74	2.92
	200002_1	141.98	83.54	41%	59%	0.32	0.32
	200002_2	797.28	563.29	29%	71%	1.22	8.97
	200003	189.7	115.38	39%	61%	0.50	0.57
	200003_1	2142.83	1336.56	38%	62%	0.76	3.71
	200003_2	121.33	67.45	44%	56%	0.35	0.31
	300001	214.46	126.81	41%	59%	0.82	1.04
	300001_1	2151.24	1362.87	37%	63%	1.21	13.86
	300001_2	307.26	214.06	30%	70%	1.43	16.33
	50000	2160.71	1291.31	40%	60%	1.68	42.23
Matrix	200006	2158.596	1320.19	39%	61%	0.70	2.51
	200007	2158.596	1342.46	38%	62%	0.73	2.48
	200008	111.62	58.48	48%	52%	0.28	0.25
	200008_1	2158.596	1126.27	48%	52%	0.51	1.95
	200008_2	1475.71	828.58	44%	56%	0.50	1.57
	200009_1	2158.596	1269.71	41%	59%	0.67	3.81
	2000010	2127.117	1097.69	48%	52%	0.57	1.30
	2000011	2127.117	1048.19	51%	49%	0.51	1.04
	2000012	2127.117	1137.18	47%	53%	0.63	1.67
	2000013	2127.117	1290.31	39%	61%	0.96	2.70
	Avg_All			41%	59%	0.75	5.48
	Std Dev_all			6%	6%	0.37	
	Avg_small			42%	58%	0.44	0.87
	Std Dev_small			5%	5%	0.19	
	Avg_small_course			42%	58%	0.76	2.95
	Std Dev_course			7%	7%	0.25	
HIP							
Matrix	20014	2130.259	1235.75	42%	58%	0.74	2.05
	20015	2130.259	1217.86	43%	57%	0.67	1.48
	20016	2130.259	1354.07	36%	64%	0.94	2.59
	20017	2130.259	1358.02	36%	64%	0.97	4.50
	20018	2130.259	1392.87	35%	65%	1.07	3.46
	20019	2130.259	1344.67	37%	63%	1.04	2.78
	20020	2130.259	1467.25	31%	69%	1.44	5.07
	20020_1	334.8704	235.00	30%	70%	1.74	1.45
	20021	2147.037	1514.30	29%	71%	1.83	12.35
	20023	2147.037	1555.93	28%	72%	2.42	38.65

Description	Image	Total Area	Accepted Area	% gamma	% gamma'	gamma' avg size (um^2)	Std Dev
HIP							
	AVG			35%	65%	1.29	
	Std Dev			5%	5%	0.56	
	Avg_small			30%	70%	1.74	1.45
	Std Dev_small						
	Avg_small_course			35%	65%	1.24	8.10
	Std Dev_course			5%	5%	0.57	
HIP + Solution HT							
Matrix	20025	2147.037	1392.53	35%	65%	0.48	3.19
	20026	2147.037	1272.29	41%	59%	0.29	0.79
	20027	2147.037	1452.02	32%	68%	0.55	3.49
	20028	2147.037	1507.82	30%	70%	0.67	7.90
	20029	2147.037	1618.86	25%	75%	1.63	15.82
	20029_1	485.1667	368.89	24%	76%	2.10	5.08
	20030	2140.741	1174.72	45%	55%	0.15	0.57
	20030_1	1044.815	520.10	50%	50%	0.11	0.09
	20031	2160.71	1315.80	39%	61%	0.33	0.99
	20031_1	111.2346	62.53	44%	56%	0.20	0.21
	20032	2155.444	1224.77	43%	57%	0.25	0.53
	20032_1	412.2222	220.87	46%	54%	0.18	0.21
	20033	2160.71	1293.83	40%	60%	0.32	0.73
	20034	2160.71	1360.29	37%	63%	0.43	1.12
	AVG			38%	62%	0.55	2.91
	Std Dev			8%	8%	0.59	
	Avg_small			47%	53%	0.16	0.17
	Std Dev_small			3%	3%	0.05	
	Avg_small_course			35%	65%	0.73	4.05
	Std Dev_course			7%	7%	0.67	

Table 6: Raw data from porosity percent analysis of standard process

As Cast			HIP			SHT		
Image	%	µm²	Image	%	µm²	Image	%	µm²
SEX100-image27.tif	**0.003355**	1376673	SEX10000.tif	3.71E-03	578604.6	SEX10055.tif	8.72E-04	578604.6
SEX100-image28.tif	0.003615	1376673	SEX10001.tif	2.62E-03	578604.6	SEX10056.tif	2.40E-03	578604.6
SEX100-image29.tif	0.002891	1376673	SEX10002.tif	4.36E-04	578604.6	SEX10057.tif	0	578604.6
SEX100-image30.tif	0.002891	1376673	SEX10003.tif	8.72E-04	578604.6	SEX10058.tif	0	578604.6
SEX100-image31.tif	0.002891	1376673	SEX10004.tif	0	578604.6	SEX10059.tif	2.18E-04	578604.6
SEX100-image32.tif	0.002891	1376673	SEX10005.tif	0	578604.6	SEX10060.tif	2.18E-04	578604.6
SEX100-image33.tif	0.003213	1376672	SEX10006.tif	1.96E-03	578604.6	SEX10061.tif	4.36E-04	578604.6
SEX100-image34.tif	0.002913	1376673	SEX10007.tif	6.54E-04	578604.6	SEX10062.tif	0	578604.6

As Cast			HIP			SHT		
Image	**%**	**µm²**	**Image**	**%**	**µm²**	**Image**	**%**	**µm²**
SEX100-image35.tif	0.002913	1376673	SEX10008.tif	2.62E-03	578604.6	SEX10063.tif	0	578604.6
SEX100-image37.tif	0.002913	1376673	SEX10009.tif	0	578604.6	SEX10064.tif	0	578604.6
SEX100-image38.tif	0.002913	1376673	SEX10010.tif	0	578604.6	SEX10065.tif	0	578604.6
			SEX10011.tif	1.74E-03	578604.6	SEX10066.tif	0	578604.6
avg	0.003036		avg	9.91E-04		avg	2.97E-04	
std dev	0.000248		std dev	0.00127735		std dev	0.000699	
avg (%)	0.304%			0.099%			0.030%	

APPENDIX D: DATA FROM MODIFIED PROCESS

Table 7: Raw data from porosity percent analysis from Modified HT #1 (1250 ºC)

4_1250ºC @ 4hrs			
	Pore Area (nm^2)	Image Area (nm^2)	Porosity %
X10000	292.59	874824.69	0.033%
X10001	14.81	874824.69	0.002%
X10002	233.33	874824.69	0.027%
X10003	0.00	874824.69	0.000%
X10004	0.00	874824.69	0.000%
X10005	567.90	874824.69	0.065%
X10006	162.96	874824.69	0.019%
X10007	0.00	874824.69	0.000%
X10008	0.00	874824.69	0.000%
X10009	0.00	874824.69	0.000%
X10010	6.17	874824.69	0.001%
X10011	0.00	874824.69	0.000%
Average	106.48		1.2E-04
std dev			0.0001961

Table 8: Raw data from porosity percent analysis from Modified HT #1 (1218 ºC)

5_1218ºC @ 4hrs			
	Pore Area (nm^2)	Image Area (nm^2)	Porosity %
X10000	6.17	874824.69	0.001%
X10001	0.00	874824.69	0.000%
X10002	0.00	874824.69	0.000%
X10003	545.68	874824.69	0.062%
X10004	193.83	874824.69	0.022%
X10005	0.00	874824.69	0.000%
X10006	191.36	874824.69	0.022%
X10007	16.05	874824.69	0.002%
X10008	230.86	874824.69	0.026%
X10009	12.35	874824.69	0.001%

5_1218ºC @ 4hrs			
	Pore Area (nm^2)	Image Area (nm^2)	Porosity %
X10010	9.88	874824.69	0.001%
X10011	53.09	874824.69	0.006%
Average	104.94		1.2E-04
std dev			0.0001797

Table 9: Raw data from porosity percent analysis from Modified HT #1 (1185 ºC)

6_1185ºC @ 4hrs			
	Pore Area (nm^2)	Image Area (nm^2)	Porosity %
X10000	258.02	874824.69	0.029%
X10001	134.57	874824.69	0.015%
X10002	0.00	874824.69	0.000%
X10004	0.00	874824.69	0.000%
X10005	2033.33	874824.69	0.232%
X10006	0.00	874824.69	0.000%
X10007	35.80	874824.69	0.004%
X10008	23.46	874824.69	0.003%
X10009	23.46	874824.69	0.003%
X10010	0.00	874824.69	0.000%
X10011	0.00	874824.69	0.000%
Average	228.06		2.6E-04
std dev			0.0006584

Table 10: Raw data from porosity percent analysis from Modified HT #2 (1250 ºC)

7_1250ºC @ 2x2hrs			
	Pore Area (nm^2)	Image Area (nm^2)	Porosity %
X10000	556.79	874824.69	0.064%
X10001	0.00	874824.69	0.000%
X10002	541.98	874824.69	0.062%
X10003	0.00	874824.69	0.000%
X10004	0.00	874824.69	0.000%
X10005	640.74	874824.69	0.073%
X10006	404.94	874824.69	0.046%
X10007	23.46	874824.69	0.003%
X10008	0.00	874824.69	0.000%
X10009	6.17	874824.69	0.001%

7_1250ºC @ 2x2hrs			
	Pore Area (nm^2)	Image Area (nm^2)	Porosity %
X10010	0.00	874824.69	0.000%
X10011	0.00	874824.69	0.000%
Average	181.17		2.1E-04
std dev			0.0002924

Table 11: Raw data from porosity percent analysis from Modified HT #2 (1218 ºC)

8_1218ºC @ 2x2hrs			
	Pore Area (nm^2)	Image Area (nm^2)	Porosity %
X10000	14.81	874824.69	0.002%
X10001	12.35	874824.69	0.001%
X10002	0.00	874824.69	0.000%
X10003	45.68	874824.69	0.005%
X10004	0.00	874824.69	0.000%
X10005	0.00	874824.69	0.000%
X10006	0.00	874824.69	0.000%
X10007	229.63	874824.69	0.026%
X10008	0.00	874824.69	0.000%
X10009	6.17	874824.69	0.001%
X10010	350.62	874824.69	0.040%
X10011	24.69	874824.69	0.003%
Average	57.00		6.5E-05
std dev			0.0001234

Table 12: Raw data from porosity percent analysis from Modified HT #2 (1185 ºC)

9_1185ºC @ 2x2hrs			
	Pore Area (nm^2)	Image Area (nm^2)	Porosity %
X10000	0.00	874824.69	0.000%
X10001	0.00	874824.69	0.000%
X10002	132.10	874824.69	0.015%
X10003	0.00	874824.69	0.000%
X10004	46.91	874824.69	0.005%
X10005	0.00	874824.69	0.000%
X10006	27.16	874824.69	0.003%
X10007	107.41	874824.69	0.012%
X10008	67.90	874824.69	0.008%

9_1185ºC @ 2x2hrs			
	Pore Area (nm^2)	Image Area (nm^2)	Porosity %
X10009	0.00	874824.69	0.000%
X10010	338.27	874824.69	0.039%
X10011	0.00	874824.69	0.000%
Average	59.98		6.9E-05
std dev			0.0001083

Table 13: Raw data for combined average porosity percent

		Porosity %		Porosity reduction from As-Cast
		Average	std dev	
1	Cast	0.304%	0.025%	
2	+HIP	0.099%	0.128%	-67.4%
3	HIP + SOL	0.030%	0.070%	-90.2%
4	1250ºC @ 4hrs	0.012%	0.020%	-96.0%
5	1218ºC @ 4hrs	0.012%	0.018%	-96.0%
6	1185ºC @ 4hrs	0.026%	0.066%	-91.4%
7	1250ºC @ 2x2hrs	0.021%	0.029%	-93.2%
8	1218ºC @ 2x2hrs	0.0065%	0.012%	-97.9%
9	1185ºC @ 2x2hrs	0.0069%	0.011%	-97.7%

Table 14: Raw data for combined average gamma prime volume fraction and average size of gamma prime

		vol. fract	std dev	avg size	std dev		
1	Cast	59%	6%	0.754	0.374		
2	+HIP	65%	5%	1.286	0.558	vol. fract reduction from As-Cast	avg size reduction from As-Cast
3	HIP + SOL	62%	8%	0.548	0.586		
4	1250ºC @ 4hrs	12%	5%	2.819	1.600	80%	414%
5	1218ºC @ 4hrs	21%	11%	5.342	2.975	66%	874%
6	1185ºC @ 4hrs	22%	8%	6.597	3.820	64%	1103%
7	1250ºC @ 2x2hrs	14%	11%	3.133	3.719	78%	471%
8	1218ºC @ 2x2hrs	34%	0.000	14.180	0.000	46%	2486%
9	1185ºC @ 2x2hrs	31%	0.000	11.880	0.000	50%	2067%

LIST OF REFERENCES

Antony, K. C., & Radavich, J. F. (1980). The Metallurgical Aspects of Hot Isostatically Pressed Superalloy Castings. *Superalloys 1980 (Fourth International Symposium)*, 257-265.

Atkinson, H. V., & Davies, S. (2000). Fundamental Aspects of Hot Isostatic Pressing: An Overview. *Metallurgical and Materials Transactions A Vol. 31A*, 2981-2998.

Black, J. T., & Kohser, R. A. (2008). *DeGarmo's Materials and Processes in Manufacturing* . Hoboken: John Wiley & Sons, Inc.

Borofka, J., R.D., K., & Tien, J. (1988). HIP Modeling of Superalloy Powders . *Superalloys 1988 (Sixth International Symposium)*, 111 - 120.

Burke, M. A.; Beck Jr., C. G.; Crombie, E. A. (1984). The Influence of Materials Processing on the High Temperature Low Cycle Fatigue Properties on the Cast Alloy IN-738LC. *Superalloys 1984 (Fith International Symposium)*, 63 - 71.

Chang, J.-C., Yun, Y.-H., Choi, C., & Kim, J.-C. (2003). Development of Microstructure and Mechanical Properties of a Ni-base Single Crystal Superalloy by Hot-Isostatic Pressing. *Journal of Materials Engineering and Performance volume 12 no. 4*, 420 - 425.

Chang, S. H., Lee, S. C., Tang, T. P., & Ho, H. H. (2006). Effects of temperature of HIP process on characteristics of Inconel 718 superalloy. *International Journal of Cast Metals Research Vol. 19 No. 3*, 175-180.

Chang, S. H., Lee, S. C., Tang, T. P., & Ho, H. H. (2006). Evaluation of HIP pressure on Inconel 718 superalloy. *International Journal of Cast Metals Research Vol. 19 No. 3*, 181-187.

Chang, S.-H., Lee, S.-C., Tang, T.-P., & Ho, H.-H. (2006). Influences of Soaking Time in Hot Isostatic Pressing on Strength of Inconel 718 Superalloy. *Materials Transactions, Vol. 47 No. 2*, 426-432.

Clemens, M. L., Price , A., & Bellows, R. S. (2003). Advanced Solidification Processing of an Industrial Gas Turbine Engine Component. *The Journal of the Minerals, Metals and Materials Society Volume 55, Issue 3*, pp 27-31 .

Harris, K; Erickson, G L; Schwer, R E;. (1984). Mar M 247 Derivations - CM 247 LC DS Alloy CMSX Single Crystal Alloys Properties & Performance. *Superalloys 1984 (Fifth International Symposium)*, 221-230.

Huang, H.-E., & Koo, C.-H. (2004). Characteristics and Mechanical Properties of Polycrystalline CM 247 LC Superalloy Casting. *Materials Transactions, Vol 45, No. 2 The Japan Institue of Metals*, 562-568.

Lamberigts, M., Diderrich, E., Coutsouradis, D., De Lamotte, E., Drapier, J. m., & Deridder, E. (1980). HIP'ing Various Precision Cast Engine Components in Nickel-Base Superalloys. *1980 (Fourth International Symposium)*, 286-294.

Lecomte-Beckers, J. (1988). Study of Microporosity Formation in Nickel-Base Superalloys. *Metallurgical Transactions A volume 19A*, 2341-2348.

Lecomte-Beckers, J., & Lamberigts, M. (1986). Microporosity Formation in Nickel Base Superalloys in Relation with thier Solidification Sequence. *Proceedings of the International Conference of High Temperature Alloys for Gas Turbine and Other Applications* (pp. 745-755). Liege: Kluwer.

McLean, M., & Tipler, H. R. (1984). Assessment of damage accumulation and property regeneration by hot isostatic pressing and heat treatment of laboratory-tested and service exposed IN738LC. *Superalloys 1984 (Fifth International Symposium)*, 73-82.

Meyers, M. A., & Chawla, K. K. (2009). *Mechanical Behavior of Materials.* Cambridge: Cambridge University Press.

Przeliorz, R., Binczyk, F., Gradon, P., Goral, M., & Mikuszewski, T. (2014). Evaluation of Heat Capacity and Resistance to Cyclic Oxydation of Nickel Superalloys. Archives of Foundry Engineering . *Foundry Commission of the Polish Academy of Sciences*, 69.

Quattrochi, D. (2006, 08 06). *3.7 Brayton Cycle*. Retrieved 02 08, 2015, from Thermodynamics and Propulsion: http://web.mit.edu/16.unified/www/SPRING/propulsion/notes/node27.html

Rajendran, R., Petley, V., & Rehmer, B. (2012). Dynamic elastic properties of aero-engine metallic isotropic materials. *Materials; Design and Applications*, 1-7.

Reed, R. C. (2006). *The Superalloys Fundamentals and Applications.* Cambridge: Cambridge University Press.

Shih-Chin, L., Chang, S.-H., Tang, T.-P., Ho, H.-H., & Chen, J.-K. (2006). Improvement in the Microstructure and Tensile Properties of Inconel 718 Superalloy by HIP Treatment. *Materials Transactions, Vol 47, No. 11* , 2877-2881.

Siereveld, P., Radavich, J. F., Kelly , T., Cole, G., & Widmer, R. (1988). Effect of HIP parameters on fine grain cast Alloy 718. *Superalloys 1988 (Sixth International Symposium)*, 459-467.

Sims, C. T., Stoloff, N. S., & Hagel, W. C. (1987). *Superalloys II.* New York: John Wiley & Sons.

Sims, Chester T.;. (1984). A History of Superalloy Metallurgy for Superalloy Metallurgist. *Superalloys 1984 (Fifth International Symposium*, 399-419.

Singh, A. R. (2011, May). *Mechanisms of ordered gamma prome precipitation in nickel base superalloys.* Retrieved 06 13, 2015, from UNT Digital Library: http://digital.library.unt.edu/ark:/67531/metadc67949/

Smallman, R. E., & Ngan, A. W. (2007). *Physical Metallurgy and Advanced Materials* . Oxford: Elsevier Ltd.

Tien, J. K., & Caulfield, T. (2015, 08 07). *Superallos, Supercomposites and Superceramics*. Retrieved 08 07, 2015, from Google Books: https://books.google.com/books?id=o0iqGb26ztgC&pg=PA99&lpg=PA99&dq=%22Metallurgy+of+Investment+Cast+Superalloy%22&source=bl&ots=AIJYOVop2s&sig=pD1NiYprqsroqelVpUi6cWl6RNs&hl=en&sa=X&ved=0CB4Q6AEwAGoVChMI963UpouXxwIVwlc-Ch11NA5A#v=onepage&q=%22Metallurgy%2

Van Drunen, G., Liburdi, J., Wallace, W., & Terada, T. (1979). Hot Isostatic Processing of IN-738 Turbine Blades. *Advanced Fabrication Processees (No. 256)* (pp. 13-1 to 13-12). London: Technical Editing and Reproduction, Ltd.

Weaver, M. L. (2011, 03 29). *Module #19 Solid Solution Hardening.* Retrieved 03 21, 2015, from http://bama.ua.edu/~mweaver/courses/MechBeh/N19.pdf

Whitesell III, H. S. (2002). *Influence of Solidification Variables on the Cast Microstructure and Porosity in Directionally Solidified Mar-M247 (Doctoral Dissertation).* Ann Arbor: Retrieved from ProQuest Dissertations and Theses. (Publication No. AAT 3057177).

Zhang, S., & Zhao, D. (2013). *Aerospace Materials Handbook.* Boca Raton: CNC Press Taylor & Francis Group, LLC.